

INVESTIGATION OF
A CHARGE TRANSFER
AT COMPLEX OXIDE INTERFACES

Author
Figen Ece Demirer

Committee
Prof. dr. ing. A.J.H.M. Rijnders
Prof. dr. ir. G. Koster
Prof. dr. P.J. Kelly
MSc. J. Geessinck

A thesis submitted for the degree of Master of Science in Nanotechnology

August 2017

List of Figures

1	A perovskite (001) interface schematic emphasizing the continuity of oxygen backbone structure and the shared octahedra at the interface (marked with the black circle). ABO_3 and $AB'O_3$ refer to two different perovskite structures. Atom representations: A (green) , B (blue) and O (red) [75].	8
2	a) Oxygen $2p$ levels align in energy when two TMOs form an interface. b) Due to potential energy difference, occupied d states at the higher potential side transfer electrons to the unoccupied d states at lower potential side. In case of charge transfer, potential energy of the charge receiving side increases causing the oxygen $2p$ levels to misalign again. [75]	9
3	This so-called simplified energy levels graph is a summary of bulk ε_p (filled data points) and ε_d (empty data points) values with respect to the Fermi level $E_F = 0$ for different $SrBO_3$ (continuous line) perovskite oxides in (001) orientation. B site elements are transition metals from $3d$ (black), $4d$ (red), and $5d$ (blue) orbitals. Dashed line (black) indicates $B = 3d$ for $LaBO_3$ perovskite oxides [75].	10
4	Graphic representations of $SrNbO_3$ and/or $SrVO_3$ containing samples grown at $SrTiO_3$ substrates. The samples are named as $y/x/y$ where y and x refer to unit cell thickness of $SrVO_3$ and $SrNbO_3$, respectively	12
5	Graphic representations of $LaMnO_3$ and/or $LaTiO_3$ containing samples grown at $LaAlO_3$ substrates. The samples are named as $(x + y)_n + a$ where x and y refers to unit cell thickness of $LaTiO_3$ and $LaMnO_3$ layers, n is the repetition number of the stack $x + y$ and a is the single top layer	12
6	Top-view representation of the PLD chamber section of the COMAT cluster including in-situ RHEED equipment [65].	14
7	The $GdFeO_3$ -type crystal structure of $LaMnO_3$, visualizing an orthorhombically distorted perovskite-type structure [62].	15
8	The $GdFeO_3$ -type crystal structure of $LaTiO_3$, an orthorhombic perovskite-type structure [15]	16
9	Annular dark-field scanning transmission electron microscopy image of $LaTiO_3$ grown at $SrTiO_3$. $La_2Ti_2O_7$ impurities are visible after 4 unit cells of thickness at (110) orientations [58]	17
11	A typical RHEED pattern obtained from a perfect $SrTiO_3$ crystal.	18
10	(a) Ewald sphere construction in 3-dimensions, (b) A section of the horizontal $z=0$ plane [64]	18
12	Schematic of typical electron energy transitions observed in XPS: (a) initial state; (b) ejection of an electron from K shell; (c) X-ray emission when $2s$ electron fills vacancy; (d) Auger electron emission, KLL transition [56]	20
13	$Mn2p$ spectra gathered from compounds Mn_2O_3 (top) and MnO (bottom) [10]	24
14	A schematic representation of the angle resolved XPS measurement. Demonstrating the sampling depth (dark gray) vs. angle of incidence [14].	25
15	$Nb3d$ core level spectra of samples (a) (b) (c), fitted with oxidation states of Nb^{+3} , Nb^{+4} and Nb^{+5} . Measurements are taken with standard angle XPS method and 50 eV pass energy is used.	27
16	(a) $SrTiO_3$ substrate @600C. (b) $SrNbO_3$ thin film on $SrTiO_3$ substrate @600C (deposition continues). (c) $SrNbO_3$ thin film on $SrTiO_3$ substrate @600C (grown 3-dimensional)	28
17	(a) Broad angle scan of the sample 0/70/0. The $SrTiO_3$ substrate (marked with blue stars) and $SrNbO_3$ (marked with red stars) peaks are visible. (b) Detailed scan of the sample 0/70/0 $SrNbO_3$ (red) compared with the $SrTiO_3$ substrate (orange) around $2\theta=45.0$ which corresponds to (002) $SrNbO_3$ (c) Detailed scan of the sample 0/70/0 peak near $2\theta=22.1$ which corresponds to (001) $SrNbO_3$	29

18	V $2p_{3/2}$ core level spectra gathered from samples (a) (b) (c), fitted with V $^{+5}$, V $^{+4}$ and V $^{+3}$ oxidation state peaks. Standard angle XPS measurement is used with pass energy of 50 eV.	30
19	XPS V $2p$ core level spectra of the sample 35/0/0 gathered by (a) standard angle measurement, (b) smaller angle measurement, fitted with V $^{+5}$, V $^{+4}$ and V $^{+3}$ oxidation state peaks. Two images	32
20	(a) Broad angle scan of the sample 35/0/0. The SrTiO $_3$ substrate (marked with blue star) and SrVO $_3$ (marked with red star) peaks are visible. (b) Detailed scan of the sample 35/0/0 SrVO $_3$ (black) compared with the SrTiO $_3$ substrate (red) around $2\theta=47.3$ which corresponds to (002) SrVO $_3$. (c) Detailed scan of the sample 35/0/0 near $2\theta=23.1$ which corresponds to (001) SrVO $_3$ Two images	33
21	Demonstration of a $\sqrt{2} \times \sqrt{2}$ surface reconstruction by orange atoms. The resulting reciprocal space map showing regular (green arrow) and additional spots (red arrow) due to surface reconstruction [1].	34
22	RHEED images taken during the deposition of the sample 2/2/2. From left to right, images follow the order of the deposition. Each image is named according to the final deposited layer, thickness and temperature. Images demonstrate conformal, epitaxial growth with constant spot separation.	35
23	Mn $3s$ core level spectra collected via standard angle XPS measurement, by using 50 eV. 36	
24	Mn $2p$ core level spectra of the samples taken at 20 eV pass energy with a standard angle. 38	
25	Mn $2p$ core level spectra of the samples $(x+y)_1+1$ (blue), $(x+y)_0+1$ (green), $(x+y)_3+0$ (red). XPS Spectra of blue and red spectra are taken at 20eV pass energy while green is taken at 50eV. Normalization of the peaks are with respect to total area under each peak.	39
26	Ti $2p$ core level spectra taken with XPS standard angle measurement with a pass energy of 50eV. Two peaks supposedly assigned to Ti $^{+3}$ (orange) and Ti $^{+4}$ (red) are fitted under the spectra.	40
27	V $2p$ level XPS spectra taken with two different angles (a) and (b). Fitted peaks are utilized for stoichiometry measurement.	48
28	AFM image of the sample 70/0/0 SrVO $_3$ taken in non-contact mode.	49
29	XPS Mn $2p$ core level spectrum of the sample. The image is presented to prove fitting model developed for Mn $^{+3}$ state is not conforming with the peak character of this sample, which is therefore predicted to contain larger Mn $^{+2}$ character	49

Contents

1	Introduction	7
1.1	Theory of Band Alignment at Oxide Interfaces	8
1.2	Purpose of the Study	10
1.3	Design of the Study	10
2	Methods	12
2.1	Substrate Preparation	12
2.2	Growth of Thin Films via Pulsed Laser Deposition	13
2.2.1	Growth of SrNbO ₃	14
2.2.2	Growth of SrVO ₃	15
2.2.3	Growth of LaMnO ₃	15
2.2.4	Growth of LaTiO ₃	16
2.3	Characterization of Thin Films	17
2.3.1	Reflection High-Energy Electron Diffraction (RHEED)	17
2.3.2	Atomic Force Microscopy (AFM)	19
2.3.3	X-Ray Photoelectron Spectroscopy (XPS)	19
3	Results and Discussions	26
3.1	Charge Transfer at SrVO ₃ /SrNbO ₃ Interfaces	26
3.2	Charge Transfer at LaTiO ₃ /LaMnO ₃ Interfaces	35
4	Conclusions	40
4.1	Conclusions on SrVO ₃ /SrNbO ₃ Interface	40
4.2	Conclusions on LaTiO ₃ /LaMnO ₃ Interface	41
4.3	Suggestions for Future work	42
5	Appendix	48
6	Acknowledgements	50

Abstract

Inspired by the theoretical work suggesting a simple method to predict the charge transfer between any chosen transition metal oxide (TMO) at their interface, this study provided experimental evidence on the charge transfer between TMO pairs of SrVO₃/SrNbO₃ and LaTiO₃/LaMnO₃. XPS core level spectra of the transition metal sites are utilized to monitor the valence changes of the transition metal sites. Valence state information gathered from the bulk and the interface sites, are compared to draw conclusions on the charge transfer at the interfaces. Due to compounds SrVO₃ and SrNbO₃ containing highly degenerate energy levels, XPS spectrum interpretation became challenging. By using final-state effects to explain the multi-peak structure appearance in XPS core level spectra of Nb and V, meaningful results on the charge transfer are gathered. Nb ion sites demonstrated a shift from Nb⁺⁴ towards Nb⁺⁵ at the interface states, suggesting charge transfer from SrNbO₃ layer to SrVO₃ layer. For LaTiO₃/LaMnO₃ pair, even though observation of a slight shift in the Mn⁺³ valence state towards the Mn⁺² was made, it could not be quantified due to the characteristic of the peak fitting method.

1 Introduction

An interface, as defined in Oxford dictionary "a surface forming a common boundary between two portions of matter or space", is a fruitful area to study the physical mechanisms that govern materials [2]. It didn't take long for scientists to start exploiting the novel electronic, magnetic and optical properties at the interfaces.

For the particular case of oxides, in which characteristic strong correlation effects influence the electron-electron (e-e), electron-lattice (e-l) interactions; rich variety of physical phenomena are accommodated at the interface that are not possible to observe in conventional semiconductor interfaces.

Key insights suggesting the presence of a surface can lead to electronic reconstruction and correspondingly novel electronic behavior, initiated theoretical studies about charge re-construction at oxide interfaces, which is still in its infancy today [27] [43]. Some of the novel physical phenomena demonstrated up to date are metal-insulator transitions [32], 2-dimensional electron gas at oxide interfaces [57], superconductors with very high transition temperatures [41] and colossal magnetoresistance [66]. The current research in oxide interfaces, focuses on the topic of controlling spin, orbital, charge and lattice degrees of freedom of strongly correlated electron systems at oxide interfaces. These degrees of freedom can be manipulated by combining specific oxides. Further tuning is proven possible by methods such as strain engineering at interfaces by arrangements in superlattice parameters [72], defect engineering at interfaces by manipulation of growth conditions [29] and by modulation doping at the interfaces by addition of a high band gap spacer layer [48].

Furthermore, the development of unit-cell precision oxide growth techniques such as Pulsed Laser Deposition (PLD) and Molecular Beam Epitaxy (MBE) enabled realization of controlled oxide interfaces in a reproducible manner.

The advancements in oxide production techniques and the ability of oxides to deliver spin, orbital, charge and lattice degrees of freedom in a single material system, caused emergence of the idea that mass-produced, multi-functional oxide materials will be the building blocks of the next generation electronic devices [30].

Coming back to the present, the challenges scientists face which slow down the further developments in the field of oxide interfaces are being addressed. Amongst them, the need for a theoretical model to explain the band alignment at oxide interfaces can be counted. Because well-established methods to study the band alignments at semiconductor interfaces such as Anderson's and the Schottky-Mott rule are failing to explain and reproduce the observed behavior at oxide interfaces.

This failure can be attributed to two assumptions. Firstly, the assumption that each oxide material has a single work function was not representative for complex oxides and was causing ill-defined band alignment in oxide interfaces: In semiconductor interfaces, when two different materials are put into contact, the work functions from both sides of the interface would align their energy levels with respect to vacuum level zero. Transition metal oxides (ABO_3) on the other hand, are composed of alternating layers of AO and BO_2 that have highly different work functions (up to 2 eV) which makes it impossible to assign a single value for each compound [74]. Secondly, the approximations implemented in the model for semiconductor interfaces were not valid for oxide interfaces due to the increased importance of microscopic interactions of strongly correlated electron systems at the oxide interfaces. As a consequence, the need for a theoretical model which includes parameters for strongly correlated electron systems in addition to better-defined alignment conditions to study the band alignment and charge reconstructions at oxide interfaces arose. The scientists were seeking after the establishment of a model to be able to simulate any hypothetical complex oxide compound combination and predict their properties, without investing on the costly, laborious experimental work that caused by trial and error.

Currently, there are few theoretical models to explain the band alignment and charge reconstructions at transition metal oxide (TMO) interfaces. The first model, developed as a hybrid form of Anderson's model for semiconductor interfaces, utilizes the electron affinity differences between the elements forming an ionic bond at each layer of the oxide (A-B, B-O-B) to model an electrostatic potential map throughout the interface [74]. The second model utilizes a parameter defined as the energy required to alter the covalence of the metal-oxygen bond in perovskite oxides, to predict the charge transfer [22]. A third model, utilizes oxygen p level alignment condition at the TMO interface to predict the

charge transfer [75]. Note that all mentioned models concern non-polar or uni-polar oxide interfaces, where the polar catastrophe effect is irrelevant.

While all models use functional theory simulations to predict the charge transfer and present the simulation results in their reports, the model presented by Zhong et al. introduces a simple prediction tool in addition to presenting simulation results. This prediction tool is a simple graph that contains information from bulk oxygen $2p$ levels of various TMOs, which Zhong et al. claim is capable of predicting charge transfer for any combination of TMOs, without the requirement of a simulation [75]. Since the promise of providing a simulation-free, fast and accessible assessment method for charge transfer is very valuable for experimentalists, the theoretical model of Zhong et al. is explained in further detail in the following section.

1.1 Theory of Band Alignment at Oxide Interfaces

This section is dedicated to the theoretical model built-up by Zhong and co-workers which explains the band alignment and charge transfer at TMO interfaces; all calculations are taken from their work [75].

The cornerstone mechanism of oxide electronics which was used in the mentioned study was the charge transfer across the TMO interfaces due to the resulting potential gradient [55] [59]. The starting point of their model was that, due to the continuous oxygen backbone structure in perovskite oxide stacks, sharing of the oxygen octahedra (marked with a black circle in Figure 1) at the interface would cause alignment of the O $2p$ levels.

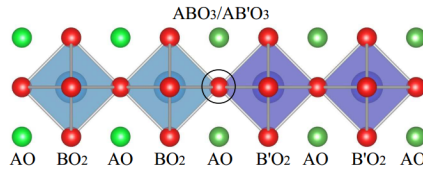


Figure 1: A perovskite (001) interface schematic emphasizing the continuity of oxygen backbone structure and the shared octahedra at the interface (marked with the black circle). ABO_3 and $AB'O_3$ refer to two different perovskite structures. Atom representations: A (green), B (blue) and O (red) [75].

Continuing with O $2p$ level alignment hypothesis they formed the following theoretical model. The O $2p$ energy level alignment would cause a difference between the Fermi levels of ABO_3 and $AB'O_3$ TMOs as seen in Figure 2 (a). The difference is equal to:

$$\Delta\varepsilon_p = \varepsilon_p^{ABO_3} - \varepsilon_p^{AB'O_3} \quad (1)$$

Since it is not physically possible to have Fermi level discontinuity at the interface, a re-arrangement was suggested which may or may not result in a charge transfer between the TMOs. In the case of Figure 1, a charge transfer happens due to electrons driven away from the partially filled d orbital states of ABO_3 towards the empty d orbital states of $AB'O_3$. The charge transfer would cause:

- An electrostatic potential drop $\Delta\phi$ across the interface,
- Rigid band shifts we indicate by $\Delta\varepsilon_{DOS}$,
- A local electrostatic potential drop $\Delta\varepsilon_{pd}$ yielding relative shifts between TM d and oxygen p .

Note that what experimentalists can measure as the band structure is the final state depicted in Figure 2(b).

It was stressed that, unlike semiconductor pn -junctions in which the only relevant term is $\Delta\phi$, a charge transfer at oxide interfaces needs to consider microscopic details for the energy balance equation, which finally determines the Δn_e . As described in Equation 2, in addition to $\Delta\phi$ term (which is the only factor for semiconductor interfaces), the charge transfer in TMOs would induce shifts in the local potentials

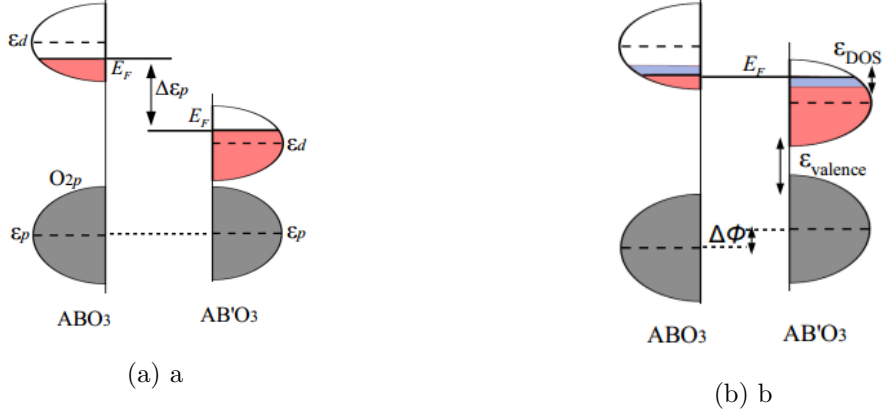


Figure 2: a) Oxygen $2p$ levels align in energy when two TMOs form an interface. b) Due to potential energy difference, occupied d states at the higher potential side transfer electrons to the unoccupied d states at lower potential side. In case of charge transfer, potential energy of the charge receiving side increases causing the oxygen $2p$ levels to misalign again. [75]

of the different transition metal (TM) sites, which can be disentangled into two contributions from (i) mutual change of the valence of B and B' sites ($\Delta\varepsilon_{dp}$) yielding relative shifts between TM d and oxygen $2p$ states with a sign equal to that of Δn_e . And (ii) from from specific structure of density of states $\Delta\varepsilon_{DOS}$ [75].

$$-\Delta\varepsilon_p = \Delta\phi + \Delta\varepsilon_{DOS} + \Delta\varepsilon_{dp} \quad (2)$$

The terms on the right hand side were linearised with respect to the amount of transferred charge, $\Delta\phi = \Delta n_e \cdot (d/\epsilon)$ where d is the effective distance of charge transfer across the interface and ϵ is the dielectric permittivity. The second term was simplified to $\Delta n_e \cdot D$ with the assumption of constant density of states around E_F . D term consisted of $D = \frac{1}{D_B E_F} + \frac{1}{D'_B E_F}$ in which B and B' denotes different TM elements on the B site. Contribution from the D was calculated to be up to 1 eV. The linearization of the last term was done considering a Hartree type of self energy $\Delta\varepsilon_{dp} \approx \Delta n_e \cdot U_H$ where U_H reflects the change of the energy due to the static single particle mean-field energy that comes from electronic Coulomb interaction. By using virtual crystal approximation, it was calculated to be on the order of 1eV for SrVO_3 . After these re-arrangements, the simplified equation was boiled down to:

$$\Delta n_e \approx -\frac{1}{(d/\epsilon + D + U_H)} \cdot \Delta\varepsilon_p \quad (3)$$

This revealed remarkable insights about the amount of predicted charge transfer. Firstly, the strength of the charge transfer was considerably larger compared to the transfer at semiconductor interfaces due to microscopic interactions and significantly smaller characteristic length scale (d/ϵ). Secondly, the strength and the sign of the charge transfer can be determined by the difference of the respective bulk oxygen $2p$ energies. By using this formula, a set of data was presented in Figure 3 which is an easy and simulation-free recipe for experimentalists to engineer heterojunctions of TMO. Since the graph presented in Figure 3 will be frequently recalled in this report, hereafter it is referred to as 'the simplified energy levels graph'.

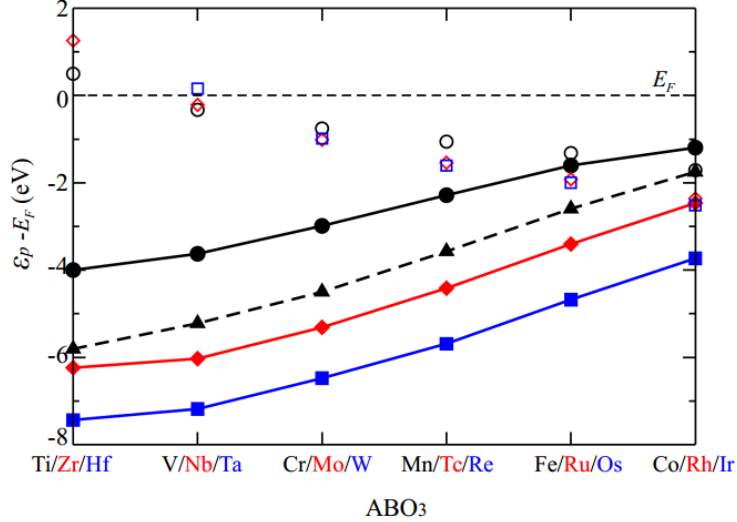


Figure 3: This so-called simplified energy levels graph is a summary of bulk ϵ_p (filled data points) and ϵ_d (empty data points) values with respect to the Fermi level $E_F = 0$ for different SrBO_3 (continuous line) perovskite oxides in (001) orientation. B site elements are transition metals from $3d$ (black), $4d$ (red), and $5d$ (blue) orbitals. Dashed line (black) indicates $B = 3d$ for LaBO_3 perovskite oxides [75].

1.2 Purpose of the Study

To our knowledge, up until now, only two works have presented experimental evidence to the band alignment and charge transfer at non-polar complex oxide interfaces [39] [22]. Both of these papers were published before the simplified guide was proposed by Zhong et al.

Considering the impact such a simple tool can have in the field of oxide design and noting that there is lack of experimental evidence to prove the validity of this tool, the work from Zhong et al. intrigued the author of this study to test the validity of the simplified method and provide experimental evidence to it.

Hence, TMO pairs utilized in this study are chosen solely by considering the information available at the simplified energy levels graph, Figure 3. The real-life versions of the modelled (or in this case "assumed") material systems are fabricated and investigated to document the expected charge transfer. By sharing the results of the observed phenomenon at the interfaces, this work aims to provide a valuable feedback to the authors on the validity of their assumptions in real, physical material systems. Providing experimental evidence that the charge transfer is indeed observed in a material design whose TMO pair is chosen from the simplified energy levels graph in Figure 3, would present the first experimental proof to their model, and mark a 'green light' to the usage of this simple method by other experimentalists.

In order for this work to provide quantitative feedback to charge transfer simulations, the author invites model developers to simulate the material systems (TMO stacks) utilized in this work and compare the findings between the two works. This quantitative feedback, is expected to provide a fine-tune to the parameters utilized in the model simulations. Note that without experimental evidence feedback, models can yield over-estimation or under-estimation results.

1.3 Design of the Study

In order to design a study that successfully examines the predicted charge transfer at TMO interfaces, an analysis of the previous work in the literature is utilized. Initially, a characterization technique that can detect the charge transfer at the TMO interfaces is searched. As previously reported, XPS [40], X-ray absorption spectroscopy (XAS) [22] and hard X-ray photo-emission spectroscopy technique utilizing synchrotron source [8] are known to yield adequate proof to the charge transfer by observing the valence state change in the transition metal sites of TMO pairs. Due to availability at the laboratory facilities, XPS technique is chosen as an investigation method for the charge transfer and

combined with PLD [63] growth technique with the desire of creating precisely grown, smooth, high quality interfaces.

Taking advantage of the presence of an in-situ reflection high-energy electron diffraction (RHEED) device implemented inside the growth chamber, thin films of desired thickness are fabricated. Since PLD and XPS chambers are connected, XPS measurements of the fabricated samples are taken without exposing the samples to the atmospheric conditions, which highly increases the reliability of the obtained results. Due to XPS being a surface sensitive technique, the interface region that needs to be monitored for a charge transfer is placed inside of a 10 nm deep data collection window thanks to growth control provided by real-time analysis of RHEED information and the precision of the PLD growth. In addition to these, growth quality is monitored by RHEED in-situ and atomic force microscopy (AFM) ex-situ. To investigate the crystal structure of the samples X-ray diffraction (XRD) technique is utilized. The realization of smooth, (001) oriented interfaces between the chosen oxide pairs is given greater care, since the expected charge transfer calculations are specifically done for (001) oriented interfaces of undistorted perovskite oxides.

1.3.0.1 Choice of Transition Metal Oxide Pairs

As presented in Section 1.1, charge transfer is expected to occur at interfaces of specific TMO pairs. In order to decide on the specific oxide pairs in which the charge transfer will be investigated, the following steps are performed. Firstly, by analyzing the simplified energy levels graph in Figure 3 together with Equations 3 and 2, pairs that are expected to yield a charge transfer are spotted. Amongst these, the pairs that acquire higher differences in their ϵ_p levels are chosen to ensure a relatively high amount of charge transfer as noted in Equation 2. Secondly, since being able to observe and prove the charge transfer via an XPS study is as important as acquiring the charge transfer itself; the oxides containing transition metals whose XPS spectra differ significantly from one oxidation state (before the transfer) to the other (after the transfer) are chosen. Finally, the *A* site elements in ABO_3 and $AB'O_3$ pairs are chosen to be the same element in order to prevent polar discontinuity throughout the interface. This restriction is made to be able to conclude that a charge transfer at the interface is solely caused by band alignment and not due to the polar catastrophe effect [57]. The same care is taken for the *A* site element choice of the substrates, since it can also cause polar catastrophe at the substrate/sample interface and affect the results badly.

As a result, complex oxide pairs of $SrRuO_3/SrFeO_3$ and $SrVO_3/SrNbO_3$ are chosen to be deposited on $SrTiO_3$ substrates and $LaTiO_3/LaMnO_3$ are chosen to be deposited on $LaAlO_3$ substrates. At later stages of the study, $SrRuO_3/SrFeO_3$ pair is abandoned due to the difficulty in fabricating smooth surfaces of $SrRuO_3$, in addition to the difficulty of preserving the Fe^{+4} oxidation state of the iron in the $SrFeO_3$ lattice.

1.3.0.2 Design of Thin Film Stacks

TMO stacks are designed to deliver clear evidence to support the aim of this study, which is investigation of a charge transfer at complex oxide interfaces.

For $SrVO_3/SrNbO_3$ containing stacks, the variation of the $Nb_{\text{interface}}/Nb_{\text{bulk}}$ ratio is taken as the main design variable. Increasing this ratio automatically increased the ratio of the information gathered from the interface Nb sites, since XPS is a surface sensitive technique with shallow sampling depth. The $Nb_{\text{interface}}/Nb_{\text{bulk}}$ ratio is varied by varying the thin film thickness of $SrNbO_3$ layer, which is sandwiched between its pair oxide $SrVO_3$. The stacks are named as $y/x/y$ in which x and y denote the unit cell thickness's of $SrNbO_3$ and $SrVO_3$ layers.

Note that the $Nb_{\text{interface}}$ representation of the stack 4(a) in an XPS measurement is 100%, while for stacks 4(b) and 4(c) this value drops down to 50% and further to 0%, respectively.

It is worth mentioning that the reason for constant thickness of $SrVO_3$ layer in each stack (except the 35 unit cell $SrVO_3$ film) is the tendency of $SrVO_3$ to grow 3-dimensional after growth of 3-4 unit cells. By avoiding thicker $SrVO_3$ layers, precise control of layer thickness by RHEED spot oscillations is guaranteed.

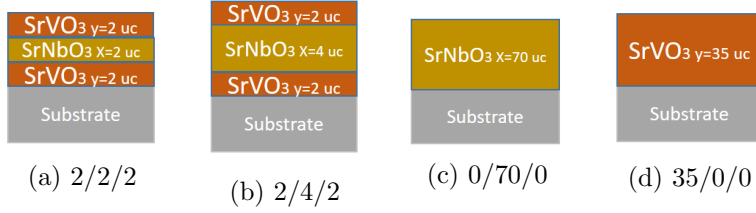


Figure 4: Graphic representations of SrNbO₃ and/or SrVO₃ containing samples grown at SrTiO₃ substrates. The samples are named as $y/x/y$ where y and x refer to unit cell thickness of SrVO₃ and SrNbO₃, respectively

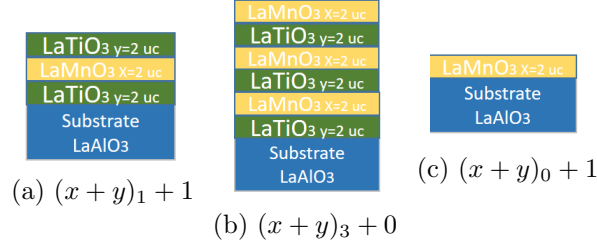


Figure 5: Graphic representations of LaMnO₃ and/or LaTiO₃ containing samples grown at LaAlO₃ substrates. The samples are named as $(x+y)_n + a$ where x and y refers to unit cell thickness of LaTiO₃ and LaMnO₃ layers, n is the repetition number of the stack $x+y$ and a is the single top layer

In parallel to this, $V_{\text{interface}}/V_{\text{bulk}}$ ratios of 50%, 50% and 0% are observed in stacks 4(a), 4(b) and 4(d), respectively.

Secondly, for LaTiO₃/LaMnO₃ containing stacks, the $Mn_{\text{interface}}/Mn_{\text{bulk}}$ ratio is taken as the design variable. However, an additional design restriction of constant stacking periodicity is introduced. This constraint is applied because of the reported result in literature [24] that, changing the periodicity in superlattices leads to a change in the lattice parameter of the deposited oxides. It is desired to avoid this change since the magnetism is strongly coupled to the lattice in LaMnO₃ materials [62] thus slight change in SrMnO₃ lattice parameter would lead to change in magnetism. As explained in Section 1.1, a change in magnetism is expected to have an impact on the kinetics of the charge transfer mechanism.

Since the periodicity of LaTiO₃/LaMnO₃ stacks are kept constant at 2 unit cells, a change in the $Mn_{\text{interface}}/Mn_{\text{bulk}}$ ratio is achieved by switching the termination (top) layer. Stacks depicted in Figure 5(a) and 5(b) show that the $Mn_{\text{interface}}/Mn_{\text{bulk}}$ ratio is decreased from 100% to 83% without changing the periodicity. Note that the $Mn_{\text{interface}}/Mn_{\text{bulk}}$ ratio of the sample in Figure 5(c) is zero, as the definition of $Mn_{\text{interface}}$ does not include the Mn at the LaAlO₃/LaMnO₃ interface since no charge transfer is predicted.

In parallel to this, $Ti_{\text{interface}}/Ti_{\text{bulk}}$ ratios of 50% and 100% are observed in stacks from Figure 5(a) and 5(b), respectively.

2 Methods

In this section, detailed information on substrate preparation, pulsed laser deposition (PLD), growth conditions and in-situ/ex-situ characterization techniques such as: AFM, RHEED, XPS and XRD are presented.

2.1 Substrate Preparation

The SrTiO₃ substrates used in this study are provided by Crystek company in (001) oriented single crystal and mixed termination (TiO₂ and SrO) state with the angle of miscut between 0.1-0.2. In

order to achieve single termination of TiO_2 , the following steps are taken. Firstly, the substrates are cleaned in low-grade ethanol and put into the sonication bath in beakers containing distilled water, for 30 minutes. This step helped oxygenation of the surface which has a vital role during the removal of the SrO termination. Later on, substrates are etched for 30 seconds in buffered HF (BHF) solution and cleaned in ethanol. The annealing is done at 950°C for 90 minutes [44].

LaAlO_3 (001) oriented substrates are utilized in mixed termination state. Substrates cleaned in ethanol bath are annealed at 950°C for 60 minutes.

Both SrTiO_3 and LaAlO_3 samples are measured with AFM after the preparations are completed in order to determine the terrace widths and heights and investigate the termination state for SrTiO_3 substrates.

2.2 Growth of Thin Films via Pulsed Laser Deposition

In this section, the chosen growth technique, PLD, is introduced and the characteristics of the utilized PLD system 'COMAT' are presented. In addition to this, the specific growth conditions chosen for each material are justified by providing a brief overview of the literature. It is implied that obtaining the correct phase, orientation and stoichiometry in the material stacks is vital to observe the predicted charge transfer. Recall that specific assumptions are made during modelling of the expected charge transfer such as (001) orientation at the TMO interfaces and undistorted cubic lattice. Therefore, all these assumptions should be implemented in the material fabrication in order to observe the expected result of charge transfer.

Even though the risk of obtaining mixed phase structures caused by distortion of the unit cell, addition of extra oxygen layers or lack of oxygen elements is reduced due to the epitaxial growth of thin films that are only a few unit cells thick; the crystal re-arrangements that can cause the above-mentioned mixed phase structures are elaborated under each section.

Pulsed Laser Deposition is a technique which uses laser ablated species from a target as particle source to grow thin film oxides in a highly controllable manner. A step-by-step description of the events taking place when the laser pulse arrives on a target surface can be presented as following, note that the time span of the described events is very short. When the laser pulse meets the target surface, it creates a dense vapour phase in front of it. As the laser pulse continues, it causes temperature and pressure of the vapour to increase, which results in partial ionization of the ablated species. The expansion of these species out of the target is described as plasma plume and it is a catastrophic event in which internal thermal and ionization energies of the species convert into kinetic energy of several hundreds of eV. Expanding plasma plume goes through various collisions with background gas particles, which causes attenuation of the kinetic energy. For this reason, ambient gas parameters such as the mass of the gas compound and the pressure determine the kinetic energies of the species arriving to the substrate. Note that by fine-tuning the properties such as the energy density at the target, pulse energy, the distance between target and substrate and the ambient gas properties; it is possible to control the growth rate and growth mode of the deposited oxides [64].

A schematic drawing of the PLD chamber of the 'COMAT' cluster can be seen from Figure 6. High pressure RHEED is added to the system for in-situ growth monitoring. An additional pump placed closer to the RHEED source allowed for monitoring even at relatively high deposition pressures (up to ≈ 300 mbar). A KrF excimer laser (Lambda Physik Compex 105, wavelength $\lambda = 248$ nm) with maximum pulse repetition rate of 50 Hz is used. The maximum pulse energy is 650 mJ with pulse duration 25 nsec. A mask is used to select the homogeneous part of the laser beam, resulting in a spatial energy variation of $\approx 5\%$ [35]. The mask is projected at an inclination of 45° on the target by means of a focusing lens (focal length 450 mm). The energy density on the target is controlled by adjustment of the attenuator.

A multi-target holder allowed mounting of up to 5 targets at a time. The mounting of target and sample holders is done through two different load locks whose pressure is kept below 10^{-6} mbar. The target holder is controlled via software for manoeuvre in XYZ directions and rotation in XY plane. Infra-red laser heating is used to increase the substrate temperature controllably with defined intervals.

Gasses that can be added to the chamber included O_2 and Ar, N_2 , He. The pressure in the deposition chamber is controlled via valve position of the main turbo valve and the gas flow parameters.

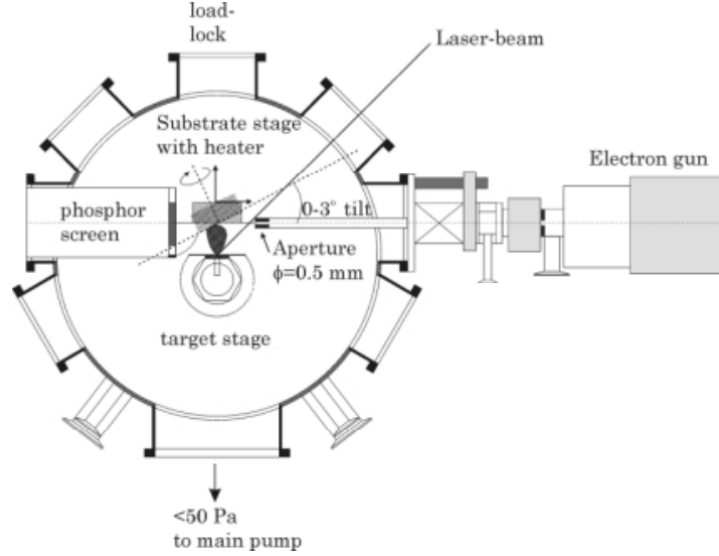


Figure 6: Top-view representation of the PLD chamber section of the COMAT cluster including in-situ RHEED equipment [65].

2.2.1 Growth of $SrNbO_3$

In the frame of this study, fabrication of stoichiometric, (001) oriented, pseudo-cubic perovskite phase $SrNbO_3$ with pseudo-cubic unit cell parameter of $a = 4.023 \text{ \AA}$ aims to be done for direct correspondance of the fabricated structure to the simulated structure described in paper by Zhong et al. [75]. Previous studies showed that Nb, Sr and O can form various compounds that all adopt perovskite-like structural features, while the most stable phase at atmospheric conditions is $Sr_2Nb_2O_7$ [34]. Although very few papers in the literature studied the growth of strontium niobate structures, they collectively mentioned that in order to prevent the formation of oxygen-rich phases such as $Sr_2Nb_2O_7$, thin films should be grown under low oxygen pressures down to 10^{-5} mbar [4][60]. In addition to this, the study by Oka et al. shown that Sr/Nb ratio of the fabricated thin films is dependent on the deposition temperature. The same study concluded that the desired stoichiometry of Sr/Nb=1 in $SrNbO_3$ compounds can be achieved by conducting PLD at 600°C [60]. Finally, amongst the studies that grow $SrNbO_3$ via PLD method, most utilized $SrTiO_3$ as a substrate [4] which has -2.93% lattice mismatch with $SrNbO_3$ while one study utilized $KTaO_3$ -0.85% lattice mismatch with $SrNbO_3$ [60].

Considering the above mentioned literature studies, the following deposition parameters are chosen for PLD of $SrNbO_3$ thin films. Firstly, despite the higher lattice mismatch, $SrTiO_3$ substrate is chosen in order to prevent additional charge transfer effects that $KTaO_3$ substrate can cause at the interface which is discussed in more detail in Section 1.3.0.1. Secondly, since low background pressures (as 10^{-5} mbar) can negatively affect the plasma plume and growth kinetics in PLD, addition of an inert gas to the chamber is decided in order to optimize the kinetic energy of the arriving particles [64]. For this reason, the deposition chamber is pumped down until the overall background gas pressure is 10^{-8} mbar and an oxygen pressure of 10^{-5} mbar is added through a needle valve. Argon gas is added to the chamber until overall pressure is $2.7 \cdot 10^{-3}$ mbar. Substrate is heated up to 600°C with a ramp rate of 50 C/min by using the infra-red heating laser. After the substrate temperature of 600°C is reached, laser pulses are shot onto the commercial sintered $SrNbO_3$ oxide target with a repetition of 1 Hz and laser fluency of 2 J/cm^2 to be deposited onto (001) oriented, TiO_2 terminated $SrTiO_3$ substrates. The target to substrate distance is fixed at 50 mm.

2.2.2 Growth of SrVO₃

In order to fabricate the exact physical structure that is simulated in the paper from Zhong et al. [75]; growth parameters for stoichiometric, (001) oriented, cubic perovskite phase of SrVO₃ with cubic unit cell parameter of $a=3.840 \text{ \AA}$ [45] are investigated. A literature search on the growth of SrVO₃ revealed that the single phase and stoichiometric SrVO₃ is difficult to grow, attributed to the high sensitivity to the oxygen background pressure [8] and tendency to acquire off-stoichiometric Sr/V ratio [33]. Previously utilized deposition parameters are summarized in Table 1 in addition to the detected phases at the end of their growth. Note that not every study which only reported SrVO₃ phase investigated the presence of secondary phase in a detailed manner.

Table 1: Deposition Parameters for SrVO₃ summarized from literature

Reference Number	Growth Method	O ₂ Pressure (mbar)	Temperature (°C)	Substrate	Present Phases
[38]	MBE	$6.7 \cdot 10^{-5}$	700	SrTiO ₃	SrVO ₃
[8]	PLD	$>5 \cdot 10^{-5}$	700	SrTiO ₃	Sr ₂ V ₂ O ₇ and SrVO ₃
[8]	PLD	$1.2 \cdot 10^{-6}$	700	SrTiO ₃	Sr ₃ V ₂ O ₈ and SrVO ₃
[68]	PLD	$1.3 \cdot 10^{-5}$	700	LaVO ₃	SrVO ₃
[42]	MBE	$2.6 \cdot 10^{-8}$	650	SrTiO ₃	SrVO ₃

Considering the findings in the literature, and the fact that SrVO₃ thin films will be deposited in an alternating manner with the SrNbO₃ thin films; it is agreed to use the exact parameters that are used for SrNbO₃ deposition in this study. Recalling that both oxides required very low oxygen pressures, keeping the temperature and background pressure constant between the depositions of alternating layers, the risk of inducing defects on the previously deposited thin films is reduced.

2.2.3 Growth of LaMnO₃

At room temperature, LaMnO₃ exhibits orthorhombic structure with GdFeO₃ type distortion (space group Pbnm). The experimentally calculated lattice parameters at 4.2 K are $a=5.742 \text{ \AA}$, $b=7.668 \text{ \AA}$, and $c=5.532 \text{ \AA}$ according to a neutron diffraction study [18]. This distorted perovskite structure has quadrupled of a perovskite unit cell with parameters of $a\sqrt{2}$, $2a$, $a\sqrt{2}$ where a is the unit cell parameter of a cubic perovskite [18].

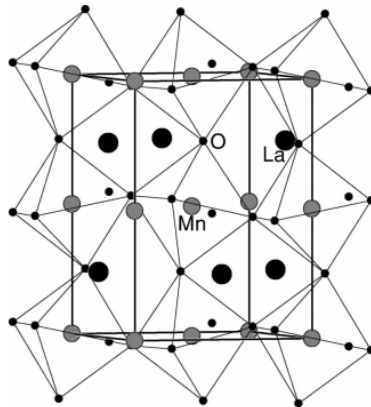


Figure 7: The GdFeO₃-type crystal structure of LaMnO₃, visualizing an orthorhombically distorted perovskite-type structure [62].

In LaMnO₃, magnetism is strongly coupled to the lattice, which causes magnetic state changes from anti-ferromagnetic to ferromagnetic to affect the arrangement of the crystal structure [62].

Stoichiometric LaMnO_3 is an insulating antiferromagnet, however it tends to demonstrate ferromagnetism when grown as thin films [51]. The reason for the ferromagnetism in thin films was found to be the cation off-stoichiometry.

A growth study showed, by using XPS measurements, that the La to Mn ratio can be improved from 0.81 to 0.92 and later on up to 0.97 when respective oxygen background pressures of $2 \cdot 10^{-1}$, 10^{-4} and $5 \cdot 10^{-6}$ mbar were used [51]. The same group studied the effect of laser fluency on the lattice parameters and found that higher laser fluencies ($\approx 2 \text{ J/cm}^2$) were more successful at achieving stoichiometric, insulating and antiferromagnetic LaMnO_3 thin films [51].

The following deposition parameters are used in this study: First, by using a needle valve, background gas pressure of the PLD chamber is arranged in such a way that it is stabilized at 10^{-6} mbar. Following this, argon gas is added until the overall gas pressure of $2.3 \cdot 10^{-3}$ is reached. LaAlO_3 substrate is heated up to 750°C with a ramp rate of $50^\circ\text{C}/\text{min}$. Laser fluency is set to be 2 J/cm^2 and 1 Hz deposition rate is utilized. After each deposition, samples are brought back to room temperature with a ramp rate of $-20^\circ\text{C}/\text{min}$. Note that the same deposition parameters are utilized for the chosen transition metal oxide pairs ($\text{LaTiO}_3/\text{LaMnO}_3$ in this case) in order to prevent defects that can occur in already deposited layers while changing the temperature or pressure parameters from one deposition to the other.

2.2.4 Growth of LaTiO_3

At room temperature, LaTiO_3 exhibits GdFeO_3 type distortion (space group Pbnm). This structure is formed via tilting of TiO_6 octahedron around the $[110]_c$ axis of cubic perovskite lattice followed by a rotation around the c axis of cubic unit cell as depicted in Figure 8 [15].

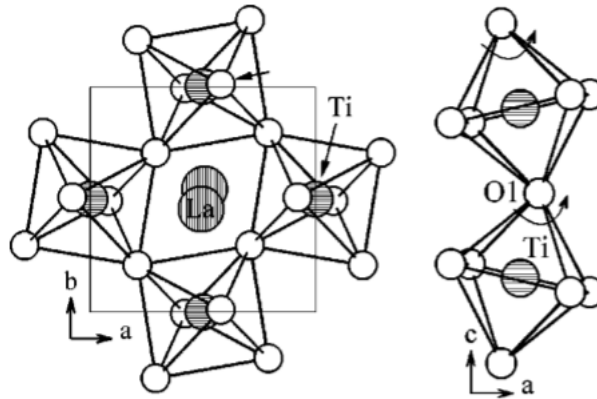


Figure 8: The GdFeO_3 -type crystal structure of LaTiO_3 , an orthorhombic perovskite-type structure [15]

The growth of LaTiO_3 was studied on substrates varying from (001)[58] to (110) [26] oriented SrTiO_3 and (001) oriented LaAlO_3 [26]. A phase transition line was observed at oxygen pressure of 10^{-4} mbar. Below this line, LaTiO_3 perovskite phase; and above, $\text{La}_2\text{Ti}_2\text{O}_7$ monoclinic phase was shown to be stabilized [59]. The formation of monoclinic $\text{La}_2\text{Ti}_2\text{O}_7$ phase occurs as explained in the perovskite derived structures section. It was shown that at low oxygen pressures where LaTiO_3 phase is stabilized, there is still $\text{La}_2\text{Ti}_2\text{O}_7$ impurities occurring at (110) orientations. A transmission electron microscopy image taken along $[100]$ axis of substrate SrTiO_3 that nicely demonstrates the dominant LaTiO_3 phase and $\text{La}_2\text{Ti}_2\text{O}_7$ impurities along $[110]$ orientation is presented in Figure 9 [58]. Important to note that the first 4 unit cells were free from phase impurities. This can be interpreted as for film thicknesses less than 4 unit cells, LaTiO_3 phase can be stabilized even at higher oxygen pressures than 10^{-4} mbar due to epitaxial constraint to the perovskite substrate [58].

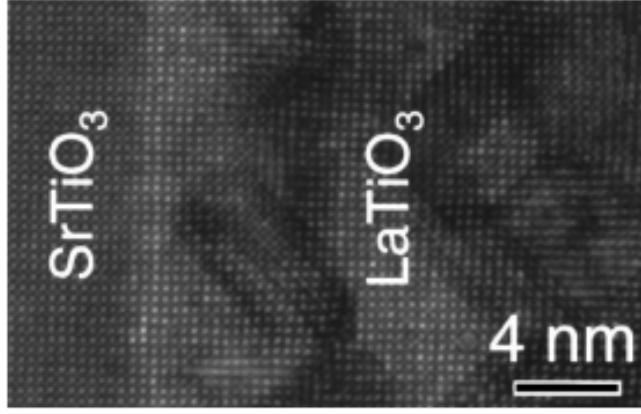


Figure 9: Annular dark-field scanning transmission electron microscopy image of LaTiO_3 grown at SrTiO_3 . $\text{La}_2\text{Ti}_2\text{O}_7$ impurities are visible after 4 unit cells of thickness at (110) orientations [58]

Using the exact same deposition parameters with the LaMnO_3 layer deposition is agreed, considering the similar requirements, such as low oxygen pressure. Thanks to the decision of keeping the temperature and the background pressure constant during depositions of alternating layers, the risk of inducing defects on the previously deposited thin films is reduced.

The following deposition parameters are used in this study. First, by using a needle valve, background gas pressure of the PLD chamber is arranged in such a way that it is stabilized at 10^{-6} mbar. Following this, argon gas is added until the overall gas pressure of $2.3 \cdot 10^{-3}$ is reached. LaAlO_3 substrate is heated up to 750°C with a ramp rate of $50^\circ\text{C}/\text{min}$. Laser fluency is set to be $2\text{J}/\text{cm}^2$ and 1 Hz deposition rate is utilized. After each deposition, samples are brought back to room temperature with a ramp rate of $-20^\circ\text{C}/\text{min}$. Note that the same deposition parameters are utilized for the chosen transition metal oxide pairs ($\text{LaTiO}_3/\text{LaMnO}_3$ in this case) in order to prevent defects that can occur in already deposited layers while changing the temperature or pressure parameters from one deposition to the other.

2.3 Characterization of Thin Films

2.3.1 Reflection High-Energy Electron Diffraction (RHEED)

Reflection High-Energy Electron Diffraction technique utilizes diffraction of electrons through surface atoms thanks to grazing angle of incidence of an electron beam onto the sample surface, and provides information about the periodic arrangement of atoms at the surface. Like in neutron diffraction and X-ray diffraction, RHEED diffraction spots appear when the momentum of the incident beam and that of the diffracted beam differ by a reciprocal lattice vector \mathbf{G} .

$$k_S - k_0 = \mathbf{G}$$

Since in elastic scattering k_S equals to k_0 , this condition results in Ewald sphere construction with radius of $2\pi/\lambda$. RHEED spots are usually gathered at $z=0$ horizontal plane where z denotes the direction normal to the sample surface. Figure 10 (a) depicts an Ewald sphere around the irradiated sample together with vertical lines which demonstrates $z=0$ horizontal plane where RHEED spots are mostly gathered from. Figure 10 (b) depicts a section of the $z=0$ plane, which is the closest to the Ewald sphere surface.

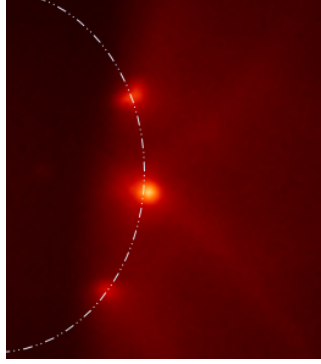


Figure 11: A typical RHEED pattern obtained from a perfect SrTiO₃ crystal.

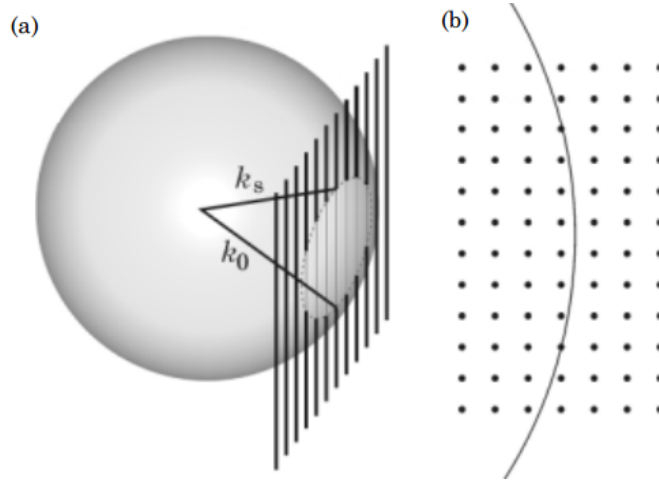


Figure 10: (a) Ewald sphere construction in 3-dimensions, (b) A section of the horizontal $z=0$ plane [64]

As depicted in Figure 11, one specular and two satellite spots are visible at grazing angle of incidence. Large energy of incoming electron beam leads to a large Ewald sphere radius, which only intersects with few reciprocal lattice rods of the grown oxides (only one rod is intersected in Figure 20(c), shown with the dotted line) at grazing angles. As a result the information one can gather from Figure 20(c) is a one-dimensional map of the reciprocal space [64].

Intensity oscillations of RHEED spots can be observed thanks to interference of the periodic initiation and coalescence of 2D islands during layer-by-layer deposition[11]. Briefly, when reactive species from plasma plume arrive to sample surface, 2D nuclei are initiated which create a disruption in the crystal potential and cause part of the diffraction beam to be out-of-phase with respect to the rest. As the process continues, coalescence of multiple 2D islands into one smooth surface returns the layer into uniform potential and restores the intensity of the spot [13]. By utilizing this feature of RHEED spots, the amount of laser pulses necessary to complete one unit cell can be calculated by measuring the amount of pulses between two peak maxima.

Observation of RHEED spot intensity change can be used to determine the growth mode as the growth continues in real-time. In theory, a perfect layer-by-layer growth would yield non-dampening intensity of oscillations. In reality, however, it is possible to observe dampening of intensity up to a degree for layer-by-layer growth on vicinal surfaces due to adsorbates starting to nucleate on top before the previous layer is completed [12]. In case a dampened specular spot intensity recovers up to some degree, a step-flow driven growth can be understood where the diffusivity of the adsorbate species increases and growth initiates only from step edges [31].

In this study, RHEED spot intensity oscillations are recorded for all samples in real-time while depositions were taking place. RHEED spots for the $z=0$ horizontal plane (a specular and two satellite) are captured before and after the growth of thin films.

2.3.2 Atomic Force Microscopy (AFM)

Commercial Atomic Force Microscopy Dimension Icon from Bruker is used to gather quantitative information about sample surfaces. Tapping mode in air is preferred and Si cantilevers are used in varying frequencies from 310 to 400 kHz in all presented AFM data.

In addition to height sensors, phase sensors collected data thanks to a four-quadrant detector. However, phase information is not used in the frame of this study. AFM imaging is done right after substrates are treated or deposited in order to minimize the contamination.

2.3.3 X-Ray Photoelectron Spectroscopy (XPS)

X-ray Photoelectron Spectroscopy (XPS), also known as electron spectroscopy for chemical analysis (ESCA) is widely utilized for analysis of surfaces.

X-ray source of XPS device radiates X-rays with energy $h\nu$, which causes photoelectric effect when absorbed by sample atoms. Electrons ejected from various electronic states travel towards the hemispherical detector with kinetic energy of E'_k . Relating the energy of absorbed X-rays ($h\nu$) to the energy of photoelectrons (E'_k), binding energy (E_b) can be calculated according to Equation 4 where ϕ_s is the work function of the sample.

$$E_b = h\nu - E'_k - \phi_s \quad (4)$$

E_b carries important information that can be used to determine the element, specific orbital and the oxidation state of the element together with the chemical environment. Binding energy information that reaches the detector is used to plot the amount of counts with respect to received binding energies. By using this graph, one can gather quantitative information about compound stoichiometry, and oxidation state ratios of elements present in a sample. Qualitatively, the chemical environment (neighbors) of elements in a sample can be deduced.

It is important to note that the information gathered in XPS measurements is extremely surface sensitive. Even though X-rays are able to excite photoelectrons from the bulk of the sample, photoelectrons generated at the bulk of the sample experience inelastic scattering on their way to escape towards the surface (vacuum) and as a result only cascade of secondary electrons that does not contain spectroscopic information reaches the detector from the bulk. In order to define a sampling depth to XPS technique, the following parameter definitions are used. Firstly, the inelastic mean free path of electrons in a solid (λ_i) is defined as the depth in which electron beam has decayed to $1/e$ its total intensity. Secondly, the sampling depth is defined as the depth from which 95% of the total amount of electrons are scattered by the time they reached the surface. Using basic algebra, the sampling depth of XPS is calculated to be $3\lambda_i$. AlK α source generates photoelectrons with inelastic mean free path of ≈ 3.5 nm which corresponds to sampling depth of ≈ 10 nm [70].

A list of electron energy transitions captured by detectors during XPS measurements is given in Figure 12. It is worth highlighting that, sharp peaks at specific binding energies stem from the accumulation of detected photoelectrons from the surface of the sample that did not lose energy due to inelastic scattering, while broad background recorded by detectors stem from secondary electrons that lost energy as they undergo inelastic collisions. Auger electrons depicted in Figure 12 (d) is due to emission followed by electron filling of a core hole.

2.3.3.1 Final-state Effects

In this study, more sophisticated aspects of XPS characterization are used as described in this paragraph. As first pointed out by Siegbahn et al., core-level binding energies are sensitive to changes in outer level (valence) charge distributions [36]. If an atom loses an electron from the valence state, its core electrons will experience an increase in the net Coulombic attraction (a product of nucleus-electron attraction and electron-electron repulsion) and their binding energies will increase. The opposite is true for an atom gaining an electron. As a result, it is possible to comment about the oxidation state of an element by analyzing the core level binding energies. Another complex event taking place during XPS measurements is the electron screening due to the created core hole [16]. When a photoelectron is generated and the sample is left with a core hole, valence electrons re-arrange and form

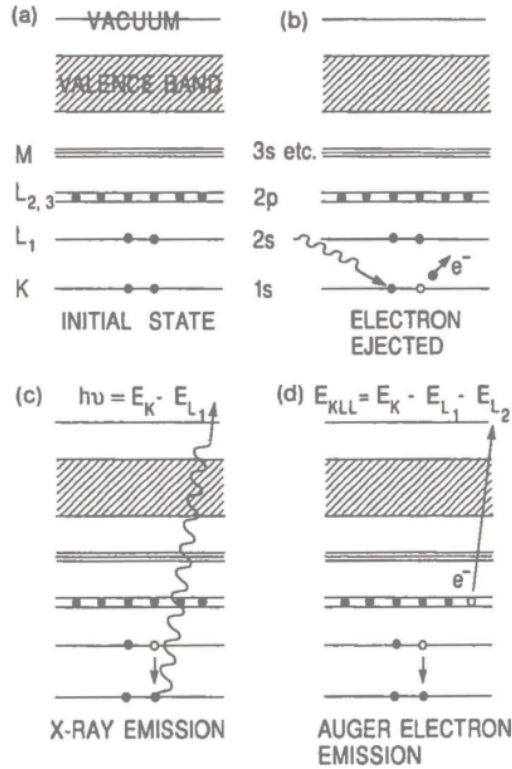


Figure 12: Schematic of typical electron energy transitions observed in XPS: (a) initial state; (b) ejection of an electron from K shell; (c) X-ray emission when 2s electron fills vacancy; (d) Auger electron emission, KLL transition [56]

a new potential equilibrium in order to screen the positively charged core hole. Since the core hole screening process is done by valence electrons, electron correlation property of the electrons in the system shapes the final arrangement. This is called final state effect because the re-arrangement of the valence electrons is triggered by the created core hole and was not intrinsic to the electron system before the emission of the core electron. The final state effect is held responsible for the appearance of three different oxidation states in XPS spectra of highly degenerate orbital system compounds, even though the sample is composed of pure phase and single oxidation state initially [47]. According to the mechanism proposed by Lin and co-workers, a created core hole triggered the re-arrangement of valence electrons that yield the observation of multi-valence peaks. Previously, compounds containing elements with highly degenerate orbitals were shown to acquire multiple oxidation states, even though the compounds were composed of a single phase and their surface was cleaned to prevent the appearance of other oxidation states [20] [49]. Lin's cluster-bath model proposal argued that the existence of multiple oxidation states for elements with highly degenerate orbitals is the result of final-state effects rather than existence of secondary phases or surface states [47].

2.3.3.2 Data Collection Procedure and Device Characteristics

Continuing with device characteristics, the XPS system used in this study is produced by Omicron Nanotechnology GmbH and equipped with an EA 125 electron energy analyzer, CN 10 charge neutralizer and a monochromized Al K α source (1486.6 eV). The calibration of the analyzer is done by using an in-situ sputter cleaned Au sample. In order to prevent charging of insulating samples, CN 10 charge neutralizer is used for insulating samples.

Samples that are fabricated at the PLD chamber COMAT are transferred to the XPS chamber while maintaining the vacuum conditions (max 10^{-8} mbar). The pressure at the XPS chamber is kept below 10^{-10} mbar.

For insulating samples, charge neutralizer is utilized with filament current of 1000 mA, emission current of 5.0 μ A and beam energy of 1.0 eV. For each sample, emission current and beam energy is

iteratively tuned to yield the best charge neutralization. This tuning remained in the range of 3-4 μA of emission current and 1-2 eV of emission current. The quality of the charge neutralization is decided according to O 1s peak measurements. The parameters yielding the minimum peak width and maximum intensity of the O 1s peak are used. The proximity of the O 1s peak to the original binding energy position of 530 eV is used as a non-priority method to further increase neutralization quality.

Pass energies varying between 20, 50, 100 eV are utilized, decided according to the desired resolution.

2.3.3.3 Information Analysis and Error Calculation

Analysis and peak fitting of the collected data is done by using CasaXPS commercial software (version 2.3.18PR1.0). Regions where the peak calculations are performed are chosen by hand and a standard Shirley background is added to this region. Shirley background is chosen because of its ability to simulate the noise created by the secondary electrons [73]. Synthetic peaks are fitted to the data. Hybrid peak profiles defined as Gaussian (Y%-Lorentzian (X%)) are shown with the notation GL(X) in CasaXPS software. The best mixture of Gaussian-Lorentzian components is dependent on the instrument and resolution (pass energy) settings used, as well as the natural line width of the specific core hole. In this study, pass energies of 20, 50 and 100 eV are utilized and the peak profile type that is used to fit the data is specified for each element under the compound sub-sections of this section. Relative Sensitivity Factors (RSF), which are band, orbital and element specific; are retrieved automatically by naming the synthetic peaks as #+element+orbital+(optionally) spin-orbit pair. RSF values are empirical values which are used to normalize the differences in the kinetics of events such as ejection from specific levels and binding to a detector such that detected peak integrals for each state will be directly proportional to the amount of states present that are giving rise to that peak in the spectra. In order to gather quantitative information such as calculation of stoichiometry and oxidation state ratios, peak areas are divided by the corresponding RSF values to correct the effects stem from above mentioned kinetics, and compared with each other.

In this study, oxidation (valence) state percentage calculations of elements Nb, V, Mn and Ti are done according to procedures explained under each compound sub-section .

Stoichiometry measurements of the compounds SrNbO_3 , SrVO_3 and LaMnO_3 are done by using samples that are thicker than the XPS sampling window and that do not contain other compound stacks in this window. These restrictions are applied considering two reasons. Firstly, in order to prevent element information from the substrates, Sr in SrTiO_3 and La in LaAlO_3 , from entering the stoichiometry analysis window. Secondly, due to the fact that even though the material thicknesses of two different compounds are the same, their relative distance to the surface will have a big impact on the representation ratios of these compounds. As a result, only the samples 0/70/0 SrNbO_3 and 35/0/0 SrVO_3 are measured, and the obtained stoichiometric ratio is assumed to be valid for their representative compound species due to unchanged deposition conditions.

Errors in calculation occur mostly due to poorly defined borders of peaks and partly due to a misfit of the fitted background with the original background, inhomogeneity of the sample compared to the spot size, spectrometer calibration errors and uncertainties in RSF values. If high precision is desired in calculations, a large number of counts can be taken in order to decrease the errors.

CasaXPS software offers a Monte Carlo simulation package for error estimates. This simulation utilizes a random number generator to create statistical noise from single measurements. It can be considered as an analogue to repeating measurements to cancel-out noise. Monte Carlo, calculates how much the noise can alter the initial fitting parameters and delivers a percentage standard deviation for each synthetic peak fitted to the data. In this study, the error calculations are done for stoichiometry measurements in addition to oxidation state ratio calculations. Since more than one peak is utilized in mentioned calculations, error division rule is applied. Assuming two peaks A and B are the only peak components of element A and B, the stoichiometry error can be calculated by using Equation 5.

$$\frac{\Delta A_{B:A}}{A_{B:A}} = \sqrt{\left(\frac{\Delta B}{B}\right)^2 + \left(\frac{\Delta A}{A}\right)^2} \quad (5)$$

Table 2: Nb3d_{5/2} binding energies and peak parameters for all oxidation states, summarized from literature.

Material	Nb3d _{5/2}									Reference
	Nb ⁺⁵ (eV)	FWHM (eV)	%	Nb ⁺⁴ (eV)	FWHM (eV)	%	Nb ⁺³ (eV)	FWHM (eV)	%	
NbO ₂ optimal oxidation [47]	207.5	1.8	55	206.5	0.9	45	-	-	-	Ag foil
NbO ₂ under-oxidation [47]	207.3	-	52	206.0	-	40	204.5	-	8	Ag foil
NbO ₂ over-oxidation [47]	207.6	1.5	62	205.9	1.1	38	-	-	-	Ag foil

In case an element or an oxidation state is composed of multiple peaks, the weighted average error is taken to be applied into the equation.

2.3.3.4 Peak Fitting Methods

SrNbO₃

Nb3d core level is chosen to be analyzed due to existing literature about peak positions, spin-orbit splitting distances and full width at half maximum (FWHM) values of this peak. After a literature review about Nb3d peak positions for different oxidation states [47] [53] [50]; Nb 3d_{5/2} peaks are placed at 207.5, 206.00 and 204.75 eV for d⁰ (Nb⁺⁵), d¹(Nb⁺⁴), d² (Nb⁺³) oxidation states, respectively. Full width at half maximum values of each spin-orbit component is set to be the same. The area ratios between Nb 3d_{5/2} and Nb 3d_{3/2} components are set to 1.66. The splitting between Nb 3d_{5/2} and Nb 3d_{3/2} is set to 2.7 eV [28].

SrVO₃

In order to determine the valence state of V in SrVO₃ samples, V 2p core level is chosen to be analyzed due to existing literature about peak positions, spin-orbit splitting distances and FWHM values of this peak. V⁺⁵ peak is reported to be at 517.9 eV while V⁺⁴ and V⁺³ follow at 516.2 eV and 514.5 eV, respectively [47]. The restrictions applied during peak fitting procedure are as follows: V 2p_{1/2} and V 2p_{3/2} spin-orbit couples are separated with 7.4eV energy between them, independent of the valence state of V [47]. FWHM values of all 2p_{3/2} peaks are constrained to be the same as 2p_{1/2} peaks [47]. Area ratio between 2p_{3/2} and 2p_{1/2} components is set to 2, corresponding to 4 electrons in the 2p_{3/2} level and 2 electrons in the 2p_{1/2} level. Respecting these constraints, three different V valence states are fitted into the data. All V 2p measurement windows included the O 1s peak due to its proximity to V 2p peak.

LaMnO₃

In order to study the oxidation state of Mn present in LaMnO₃ lattice, Mn 2p core level peaks (spin-orbit couple at binding energy range of 636-656 eV) and Mn 3s level peaks (peak couple at binding energy range of 95-105 eV) are chosen.

To start with the Mn 2p peak fitting, the multiplet splitting of Mn 2p_{3/2} core level peaks caused the fitting procedure to become a research requiring sub-project in itself. After an analysis of papers dedicated to fitting of Mn 2p_{3/2} peak, the method of utilizing sets of smaller peaks with pre-defined energy range, separation and width [54] [10] is chosen over the method of introducing a single peak with pre-defined asymmetry conditions [9] because the former design's modular structure would allow for later modifications of variables (such as FWHM parameter change that might be necessary due to a difference in instruments or simply a difference in the utilized pass energy).

Before proceeding to the details of the Mn 2p peak fit procedure, it is key to remark the importance of the fit parameters. The electron transfer from LaTiO₃ to LaMnO₃ layer is expected to cause appearance of Mn⁺² oxidation states in LaMnO₃ thin films. As Mn⁺² and Mn⁺³ states co-exist in the film, it is vital for this project to differentiate between them. Literature points out at the appearance of an additional peak at higher binding energy side of Mn 2p_{3/2} peaks, named as satellite [37][54]

Table 3: $V2p_{3/2}$ binding energies and peak parameters, summarized from literature.

Material	$V2p_{3/2}$		O1s		Δ (eV)	BE Reference
	BE (eV)	FWHM (eV)	BE (eV)	FWHM (eV)		
V_2O_5	516.9 [67]	1.6	529.8	1.7	12.9	E_{Fermi}
	517.0 [52]	1.4	529.8	1.6	12.8	O1s at 529.8 eV
	517.7 [69]	0.9	530.5	1.1	12.8	C1s at 284.6 eV
VO_2	515.65 [52]	4.0	530.0	2.8	14.3	O1s at 530.0 eV
	516.0 [17]	1.95	-	-	-	C1s at 285.0 eV
	516.2 [67]	3.2	529.9	1.8	13.7	E_{Fermi}
V_2O_3	515.2 [52]	4.8	530.0	2.0	14.8	O1s at 530.0 eV
	515.7 [67]	4.9	530.1	1.6	14.4	E_{Fermi}
	515.9 [17]	-	-	-	-	C1s at 285.0 eV
$SrVO_3$ V^{+5}	517.9 [47]	-	530.0	-	12.1	O1s at 530.0 eV
$SrVO_3$ V^{+4}	516.2 [47]	-	530.0	-	13.8	O1s at 530.0 eV
$SrVO_3$ V^{+3}	514.5 [47]	-	530.0	-	15.5	O1s at 530.0 eV

 Table 4: Peak fitting model for Mn^{+2} and Mn^{+3} for manganese oxides

Valency	Δ_{2-1}	Δ_{3-2}	Δ_{4-3}	Δ_{5-4}	FWHM	Δ_{6-5}	FWHM
Mn^{+2}	0.97	0.93	0.95	1.14	1.23	1.75	3.5
Mn^{+3}	1.10	1.27	1.50	1.62	1.75	-	-

[61] or shake-up peak [10] [21]. Formation of a satellite or shake-up peak occurs for both spin-orbit components of Mn 2p, however, due to the lack of intensity, the one near Mn $2p_{1/2}$ side is not resolved [9]. Even the shake-up peak of Mn $2p_{3/2}$ is hard to spot in case of mixed valency, some studies report Mn^{+2} states without an apparent shake-up or satellite structure and do not include an extra peak in their peak fittings [7] [6] [5]. For this reason, it is important not to rely solely on the shake-up peak feature in order to monitor the oxidation state. Luckily, Mn 2p spectra acquires multiplet splitting proposed by Gupta et al. [23] which yields different main peak structure for Mn^{+3} and Mn^{+2} states and can be used for identification. Figure 13, taken from the paper of Biesinger et al. [10] presents the Mn 2p spectra from MnO and Mn_2O_3 compounds. Mn^{+2} has slightly lower binding energy for Mn $2p_{3/2}$ peak and its slope is steeper on the lower energy side. Biesinger and co-workers utilized the theoretical work on multiplet splitting [23] to create sets of peaks with defined separations and width that yield correct reconstruction of the Mn 2p spectra.

Due to its success in defining the characteristic peak shape of Mn $2p_{3/2}$ peak in Mn^{+3} and Mn^{+2} states as seen in Figure 13, the peak fitting method is taken from the work of Biesinger et al. [10].

Table 4 shows the restrictions followed during Mn 2p peak fitting in this study. Firstly, the details for Mn^{+2} state are described as following: The set of six peaks in which five of them shared the same FWHM value of 1.23 eV (for 20 eV pass energy) are placed according to the separations noted in Table 4. The shake-up feature is defined as the sixth peak and assigned FWHM value of 3.5 eV. Its location is assigned to 6.67 eV higher than the first component of the peak set.

Secondly, the details for Mn^{+3} state peak fitting are described as following: The set is composed of five peaks which all shared the FWHM value of 1.75 eV (for 20 eV pass energy) and their spatial separations are restricted to the values shown in Table 4.

As an additional method for Mn oxidation state determination, Mn 3s peak splitting is analyzed.

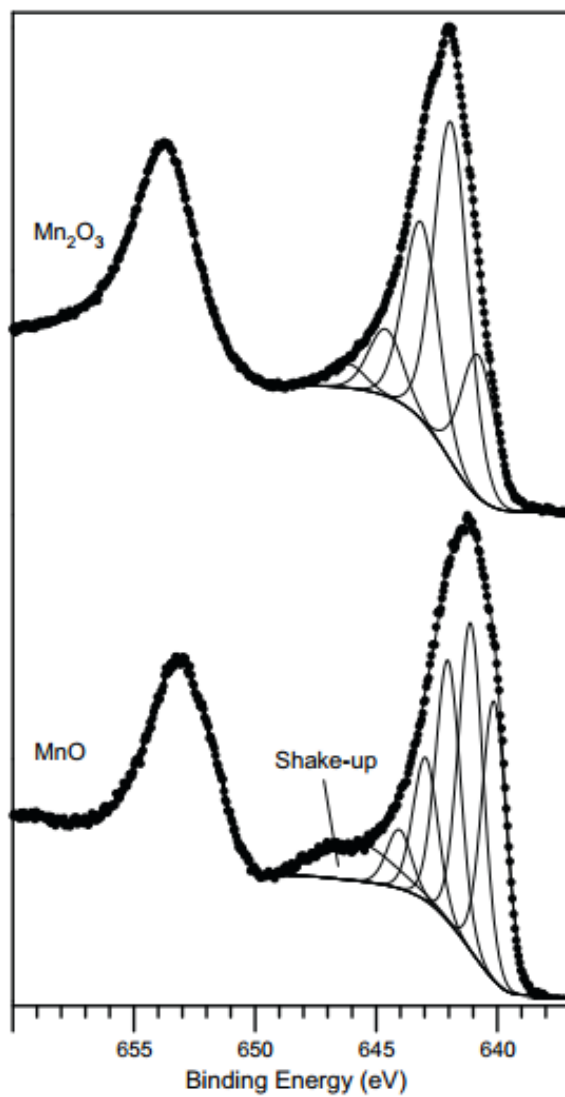


Figure 13: Mn_{2p} spectra gathered from compounds Mn₂O₃ (top) and MnO (bottom) [10]

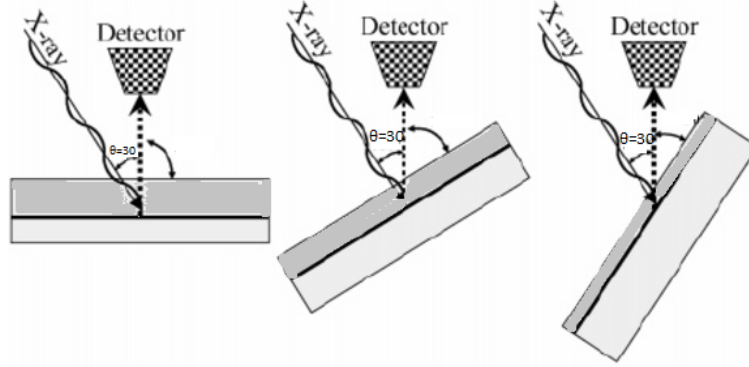


Figure 14: A schematic representation of the angle resolved XPS measurement. Demonstrating the sampling depth (dark gray) vs. angle of incidence [14].

Unlike spin-orbit coupling, Mn 3s splitting is caused by coupling of a hole in atom's subshell to an empty valence subshell [19]. For this reason, the distance between two Mn 3s peaks carries information about the valence state of the Mn atom. Beyreuther et al., utilized data gathered from literature to create an empirical relation between Mn 3s splitting and corresponding Mn valence states as presented in Equation 6 [9].

$$\nu_{\text{MN}} = 9.67 - 1.27\Delta E_{3s}/\text{eV} [9] \quad (6)$$

Finally, Mn 3s peak splitting is calculated by fitting two peaks below the spectra and determining the distance between these two peaks.

LaTiO₃

Ti 2p core level is chosen to be analyzed to monitor Ti oxidation state in LaTiO₃ material. Charging effect due to insulating LaTiO₃ material is overcome by using a neutralizer during XPS measurements. Unfortunately this led to inhomogeneous shifts in binding energies which could not be fixed by calibrating the O 1s peaks to 530 eV. As a result, the exact binding energies for Ti peaks are not taken as reference; instead, the energy separation between the oxidation state peaks is utilized. In the work by Lin et al., the Ti 2p_{3/2} peak was fitted by Ti⁺⁴ and Ti⁺³ compounds positioned at 456.9 and 455.4 eV with 1.5 eV energy separation between them. The condition of 1.5 eV separation is taken from this study [47]. FWHM values of all peak components were reported to be 1.7 eV for 20 eV pass energy, so this condition is also added to the peak fitting model. Spin-orbit splittings of all three oxidation states were reported to be 5.6 eV. and the area ratios between Ti 2p_{3/2} and Ti 2p_{1/2} components were set to 2 [47]. However, the exact peak positions reported by Lin et al. were found to be in conflict with what was reported by Kleibeuker et al. (458.4 and 458.9 eV for 2p_{3/2}Ti⁺⁴ and Ti⁺³, respectively) [39].

2.3.3.5 Angle Resolved Measurements

The detector and X-ray source are at fixed positions inside the XPS chamber and the sample holder can rotate around its axis as seen from Figure 14. This design is utilized to gather information from different depths of the material by changing the substrate angle. Recalling the escape depth of the photoelectrons generated inside the material, only the ones whose trajectories are less than inelastic mean free path can escape from the material and reach the detector. Referring to the XPS data collection window depth of ≈ 10 nm at vertical angle between detector and the sample, one can calculate the sampling depth for any angle setting. However it is worth noting that since the detector is at a fixed position, angle variation between the X-ray and sample surface is restricted. In the frame of this study, X-ray-sample surface angles of 30 and 15 degrees are utilized. The 30 degrees angle, also named standard angle, is utilized unless otherwise is mentioned. 15 degrees angle is referred to as shallow angle or smaller angle.

3 Results and Discussions

3.1 Charge Transfer at SrVO₃/SrNbO₃ Interfaces

The design of thin film stacks that contain SrVO₃/SrNbO₃ interfaces considered design parameters such as Nb_{interface}/Nb_{bulk} ratio as explained further in detail in Section 1.3.0.2. Growth parameters are kept constant for SrVO₃ and SrNbO₃ parts of the stack in order to prevent the defects that can form during layer alternation and the details of growth parameters are explained in Sections and , respectively.

First, in order to investigate the Nb oxidation state in fabricated samples, detailed XPS spectra near binding energies of Nb 3*d* core levels (212-214 eV) are collected. Synthetic peaks which correspond to Nb⁺⁵, Nb⁺⁴ and Nb⁺³ are fitted into the collected spectra by respecting restrictions described in Section 2.3.3.4. Results are presented in Figure 15 (a) (c) (b). Color-coding of this peak fitting procedure is chosen as follows: green-blue peak set is assigned to Nb⁺⁵ oxidation state while orange-yellow and pink-purple peak sets are assigned to Nb⁺⁴ and Nb⁺³ oxidation states, respectively.

As the element loses electrons from its valence shell, appearance of peaks at higher binding energies is observed that is attributed to an increase in the net Coulombic attraction (which is the product of nucleus-electron attraction and electron-electron repulsion).

Oxidation state distributions of Nb sites present in SrNbO₃ lattice are calculated by taking the area under each oxidation peak set in Figure 15 and dividing by their corresponding RSF values. The calculated percentage distributions are presented in Table 5. Error calculations presented in this table are done according to the method explained in Section 2.3.3.3 by using the input gathered from Monte Carlo simulation package in CasaXPS software. While the table only contains the relevant errors, standard deviation percentages calculated for each peak type and the oxidation state percentage are given in the Appendices section, Tables 9 and 10, respectively.

The Nb oxidation state distribution of the sample 0/70/0 exhibited 31.0±0.5% Nb⁺⁵ , 55.5±0.9% Nb⁺⁴ and 13.6±0.6% Nb⁺³ as seen in Table 5. This result is expected to be caused by final-state effects in XPS measurements which is due to the highly degenerate orbital system of SrNbO₃ behaving in such a way that after creation of a core hole by incoming X-rays, the valence electrons re-arrange themselves to screen the core hole, causing the appearance of multiple valence state peaks in the XPS spectra. Final-state effect is explained in further detail in Section 2.3.3.1. In order to investigate if there are other phases or defects present in the sample 0/70/0 which might also lead to appearance of multiple Nb oxidation states, following characterization methods are utilized.

First, stoichiometry calculations of the sample 0/70/0 are done by using O 1s, Nb 3*d* and Sr 3*p* peaks. The results revealed O/Nb and O/Sr ratios of 3.02 ± 0.05 and 2.54 ± 0.04. These results indicated two scenarios. Firstly, oxygen and Nb vacancies and secondly, excess Sr in the lattice. Both scenarios account for the Nb⁺³ presence amongst the other oxidation states present in the spectra. The paper that provided experimental evidence to final-state effects in NbO₂ compounds, supported this finding by documenting that, a fully stoichiometric NbO₂ only contains 55% Nb⁺⁵ and 45% Nb⁺⁴ while slightly oxygen deficient compound would yield 52% Nb⁺⁵, 40% Nb⁺⁴ and 8% Nb⁺³ [47].

Second, XRD measurement of the sample 0/70/0 is taken. Full spectra is presented in Figure 17(a) while close-up plots around (002) and (001) orientations of SrNbO₃ phase are presented in Figure 17 (b) and (c), respectively. No sign of secondary phase compound that contains Nb⁺⁵ (such as Sr₂Nb₂O₇) has been found. Note that considering 28 nm thickness of the sample 0/70/0, presence of a 31.0 ± 0.5% Nb⁺⁵ would be visible in XRD measurements.

Third, RHEED images presented in Figure 16 showed that, growth of SrNbO₃ in Figure 16(b) is fully epitaxial, conforming with the SrTiO₃ substrate shown in Figure 16(a). No changes in the unit cell parameters that would be expected for oxygen-rich phases such as Sr₂Nb₂O₇ is observed. Distance between RHEED spots remained constant and no additional spots appeared which is enough to conclude the structure remained the same as discussed in Section 2.3.1. Streaky pattern (horizontal elongation of RHEED spots) is caused by surface roughening. As seen in Figure 16(c), towards the end of the deposition, as the amount of added unit cells increase, growth mode become 3-dimensional. We note that it is not possible to investigate a possible crystal parameter change from the 3-dimensional

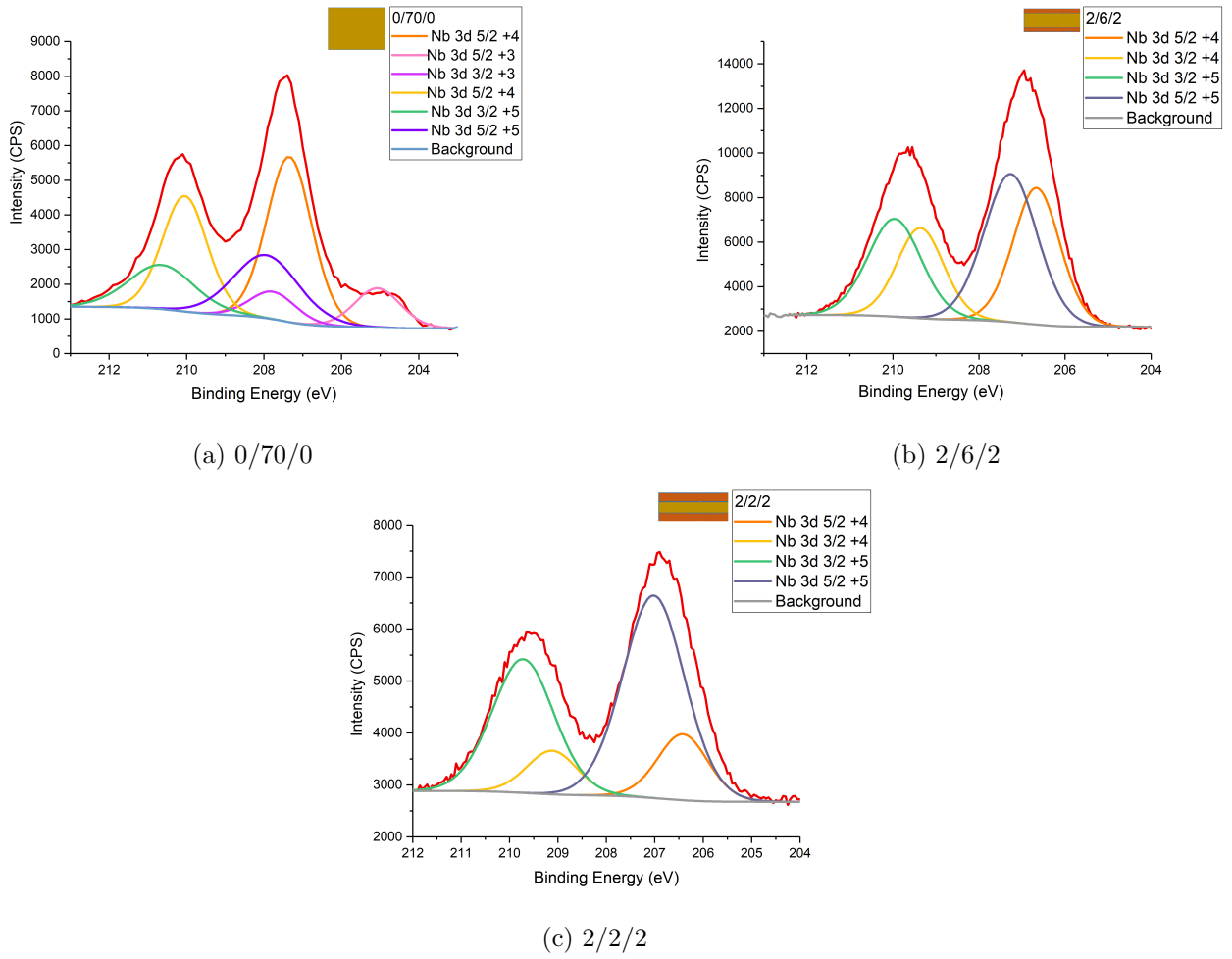


Figure 15: Nb3d core level spectra of samples (a) (b) (c), fitted with oxidation states of Nb⁺³, Nb⁺⁴ and Nb⁺⁵. Measurements are taken with standard angle XPS method and 50 eV pass energy is used.

	y/x/y	Nb ⁺⁵ %	Nb ⁺⁴ %	Nb ⁺³ %
	0/70/0	31.0 ± 0.5	55.5 ± 0.9	13.6 ± 0.6
	2/6/2	53.3 ± 4.1	44.7 ± 3.5	-
	2/2/2	78.9 ± 13.8	21.1 ± 3.5	-

Table 5: Percentage distributions of Nb oxidation states calculated from XPS Nb3d core level spectra of each sample

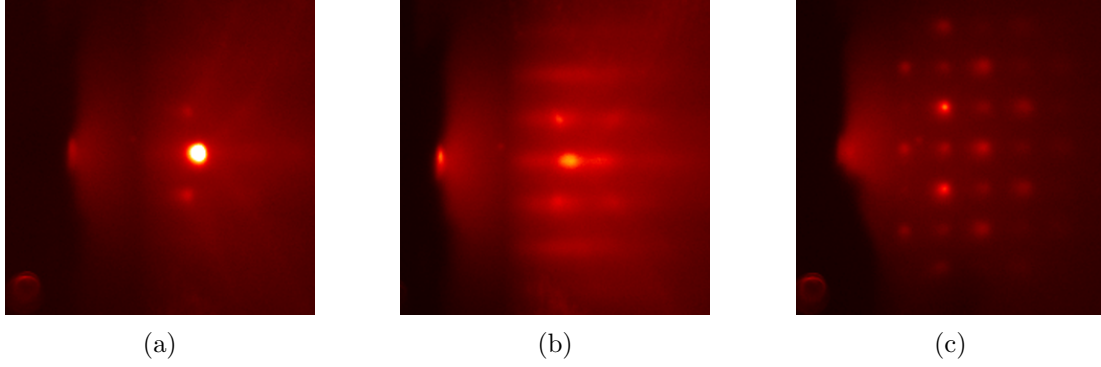


Figure 16: (a) SrTiO₃ substrate @600C. (b) SrNbO₃ thin film on SrTiO₃ substrate @600C (deposition continues). (c) SrNbO₃ thin film on SrTiO₃ substrate @600C (grown 3-dimensional)

RHEED pattern.

In the light of these findings, we conclude that Nb oxidation state distributions for the sample 0/70/0 are partly due to final-state effects and partly due to oxygen deficiency (presence of Nb⁺³). As mentioned in Section 2.3.3.3 the stoichiometry analysis is only possible for the 0/70/0 sample amongst SrNbO₃ containing stacks. An assumption is made stating that the sample 0/70/0 is stoichiometry-wise representative for thinner films (2/6/2 and 2/2/2), unless the growth conditions are altered.

Proceeding with the analysis of Nb oxidation state distributions in Table 5, considering the final-state effects play role in all the samples, one would expect to find a consistent Nb valence distribution. To explain further, the electronic transitions taking part in the core hole screening phenomenon, which causes re-arrangement of the valence electrons and correspondingly the appearance of multiple oxidation peaks, are occurring in large amount of repetitions per second. Therefore, the statistical distribution of events taking place during the core hole screening event would be expected to yield the same oxidation state distribution for all the samples, assuming that their stoichiometry is similar since the growth conditions are unchanged. However, the results summarized in Table 5 showed that this is not the case. Going from stack 0/70/0 towards 2/2/2, the percentage of Nb⁺⁵ oxidation state in the material increases, while Nb⁺⁴ percentage decreases.

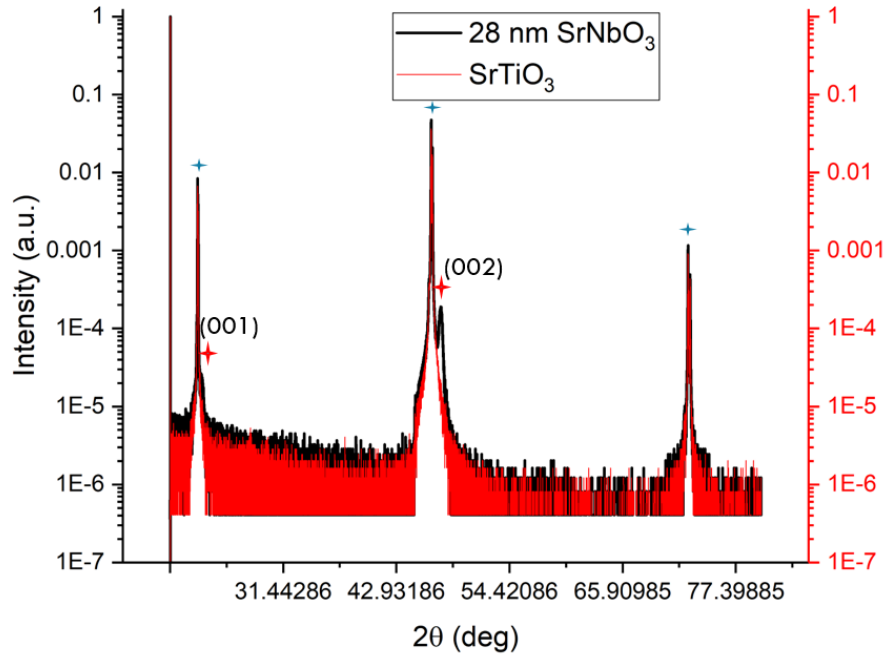
The reason behind the inconsistency of the oxidation state distributions in samples 0/70/0, 2/2/2 and 2/6/2 is claimed to be the electron transfer at the interface as the Nb⁺⁵ oxidation state percentage increases with increasing Nb_{interface}/Nb_{bulk} ratio in samples.

Let's elaborate more on this by recalling the Section 1.1. Band alignment theory at transition metal oxide interfaces discusses that the formation of an interface between SrNbO₃ and SrVO₃ results in sharing of an oxygen octahedra at the interface and forces oxygen *p* bands of two different oxides to align at the point of contact[75]. Due to this alignment, an abrupt potential difference between *d* bands of the two oxides occurs at the interface, which drives electrons from partially filled *d* orbital states of SrNbO₃ towards the empty *d* orbital states of SrVO₃. For this reason, the oxidation state of Nb⁺⁴ in SrNbO₃ lattice is expected to increase and show higher Nb⁺⁵ character as the Nb_{interface}/Nb_{bulk} ratio increases. The expected recipient of the charge, V on the other hand, is expected to reduce from V⁺⁴ towards V⁺³ at the interface.

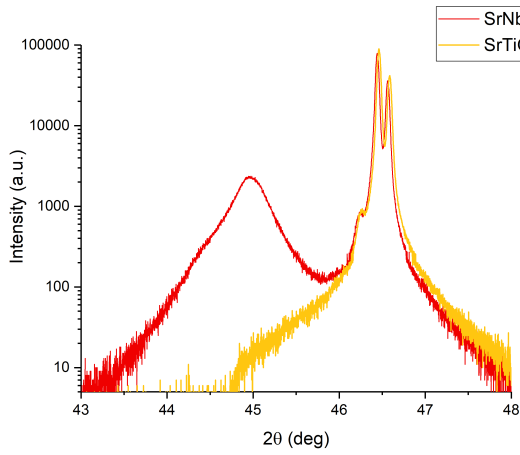
As seen in Table 5, increasing the Nb_{interface}/Nb_{bulk} ratio from 50% in sample 2/6/2 to 100% in sample 2/2/2, causes an increase from 53.3 ± 4.1% to 78.9 ± 13.8% Nb⁺⁵ oxidation state, respectively.

In order to investigate a possible charge transfer on the other side of the interface, oxidation state distributions of V in above mentioned samples are analyzed. XPS spectra is collected at binding energy range of 534-512 eV. In this range, V 2*p* core levels (527-512 eV) are captured at the same measurement window as O 1*s* level (528-530 eV).

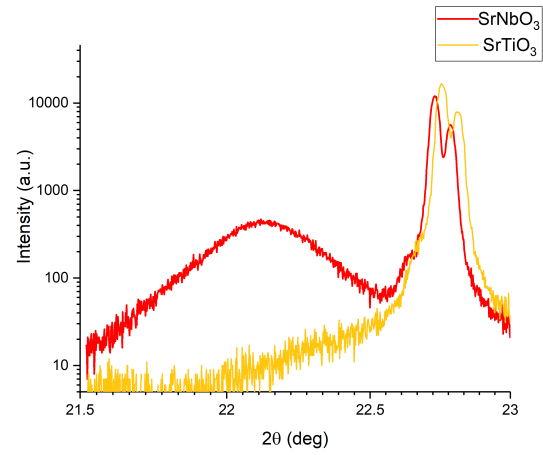
Peak fitting is done according to the rules and restrictions described in Section 2.3.3.4, considering both V2*p*_{1/2} and V 2*p*_{3/2} peaks. In order to calculate the oxidation state distributions however, only V 2*p*_{3/2} peaks are utilized for the sake of simplicity.



(a)

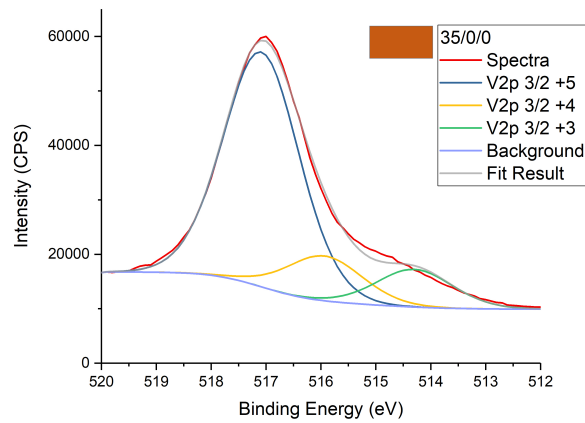


(b)

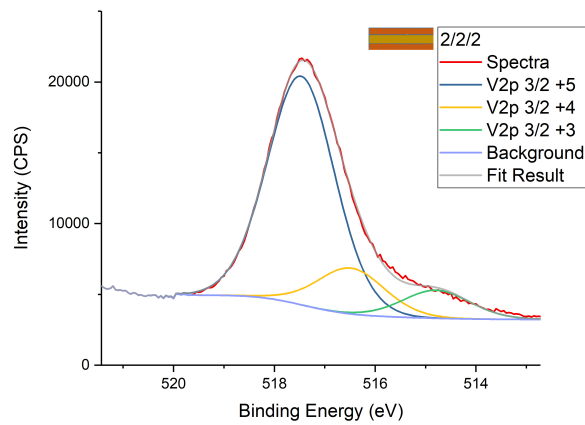


(c)

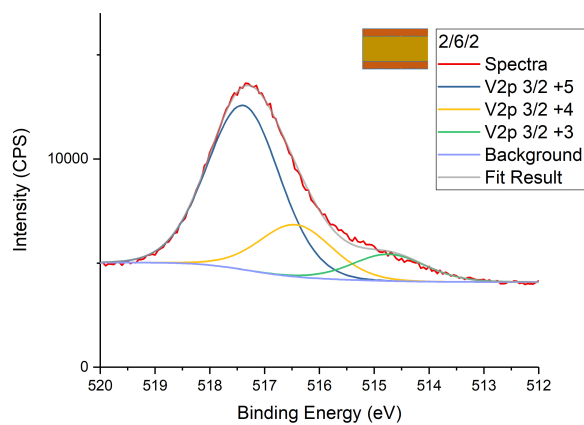
Figure 17: (a) Broad angle scan of the sample 0/70/0. The SrTiO_3 substrate (marked with blue stars) and SrNbO_3 (marked with red stars) peaks are visible. (b) Detailed scan of the sample 0/70/0 SrNbO_3 (red) compared with the SrTiO_3 substrate (orange) around $2\theta=45.0$ which corresponds to (002) SrNbO_3 (c) Detailed scan of the sample 0/70/0 peak near $2\theta=22.1$ which corresponds to (001) SrNbO_3



(a) 35/0/0



(b) 2/2/2



(c) 2/6/2

Figure 18: $V2p_{3/2}$ core level spectra gathered from samples (a) (b) (c), fitted with V^{+5} , V^{+4} and V^{+3} oxidation state peaks. Standard angle XPS measurement is used with pass energy of 50 eV.

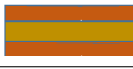
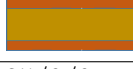
SrVO ₃ (y unit cell)	y/x/y	V ⁺⁵ %	V ⁺⁴ %	V ⁺³ %
SrNbO ₃ (x unit cell)	2/2/2			
SrVO ₃ (y unit cell)		82.4 ± 0.1	10.9	8.16
Substrate SrTiO ₃	2/6/2			
		76.0 ± 0.3	15.9	8.16
	35/0/0			
		74.0 ± 0.1	14.1	11.9

Table 6: Percentage distributions of V oxidation states calculated from XPS V2*p* core level spectra of each sample.

Angle (deg.)	V ⁺⁵ (%)	V ⁺⁴ (%)	V ⁺³ (%)
30	74.0 ± 0.1	14.1	11.9
15	89.4 ± 0.2	5.97 ± 0.01	4.67

Table 7: V oxidation state distributions calculated from XPS V2*p* core level spectra of the sample 35/0/0 by using angle resolved XPS.

As seen from Figures 18 (a), (b) and (c); all samples containing V, demonstrated coexistence of three different oxidation states: V⁺⁵ (blue), V⁺⁴ (yellow) and V⁺³ (green). By using the area of the fitted peaks, percentage contributions from each V oxidation state is calculated as shown in Table 6. Error calculations are done according to the method explained in Section 2.3.3.3 by using the input gathered from Monte Carlo simulation package in CasaXPS software. While the table only contains relevant errors, standard deviations calculated for each peak type and the oxidation state percentage are given in the Appendices Section 5, Tables 9 and 10, respectively.

In order to investigate the causes of V oxidation state distributions in the sample 35/0/0, the same procedure as Nb oxidation state determination is followed.

First, stoichiometry calculations of the sample 35/0/0 are done by using O 1*s*, V 2*p* peaks. The results revealed O/V ratio of 4.0. Excess oxygen is found in the sample which results in V⁺⁵ oxidation state. Considering 10⁻⁵ mbar of oxygen background pressure, finding of the oxygen-rich phase was unexpected. However, further literature search revealed that, formation of an oxygen-rich face at the surface of the SrVO₃ films grown under low oxygen pressures were reported in XPS measurements, even though the samples were not taken out of the vacuum throughout all the measurements [8]. In order to investigate a surface phase as suggested by the paper angle resolved XPS spectra of the sample 35/0/0 are taken.

Angle resolved XPS spectra of the sample 35/0/0 that contains 35 unit cells (14 nm) of SrVO₃, are presented in Figure 19(a) and 19(b). The angle between the incident X-ray beam and the sample surface is varied from 30 degrees¹ to 15 degrees². Stoichiometry analysis of this sample calculated with the smaller angle XPS measurement revealed O/V ratio of 4.2, while as mentioned earlier this ratio was 4.0 for standard angle measurement. Stoichiometry analysis are done by using the fitted peaks shown in Appendices, Figures 27 (a) and 27 (b), respectively. In addition to these, V oxidation state distribution calculations are done by using standard and smaller angle XPS measurements of the same sample. Distributions of V oxidation states are presented in Table 7 for standard and smaller angle measurements.

A sharp increase in Nb⁺⁵ percentage from 74.0 ± 0.1% to 89.4 ± 0.2% is observed as the measure-

¹Referred to as the standard angle

²Referred to as the smaller angle

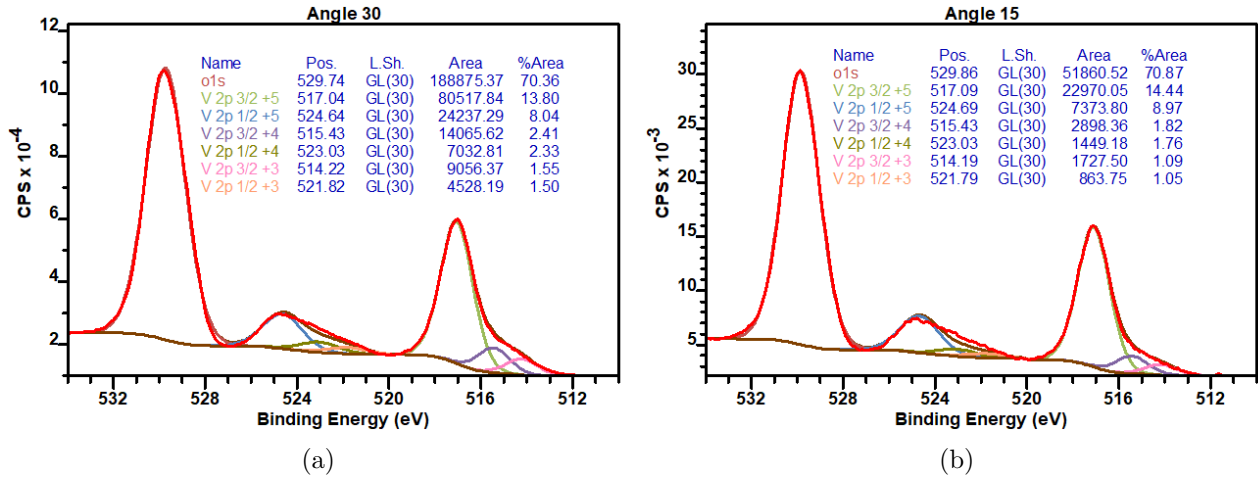
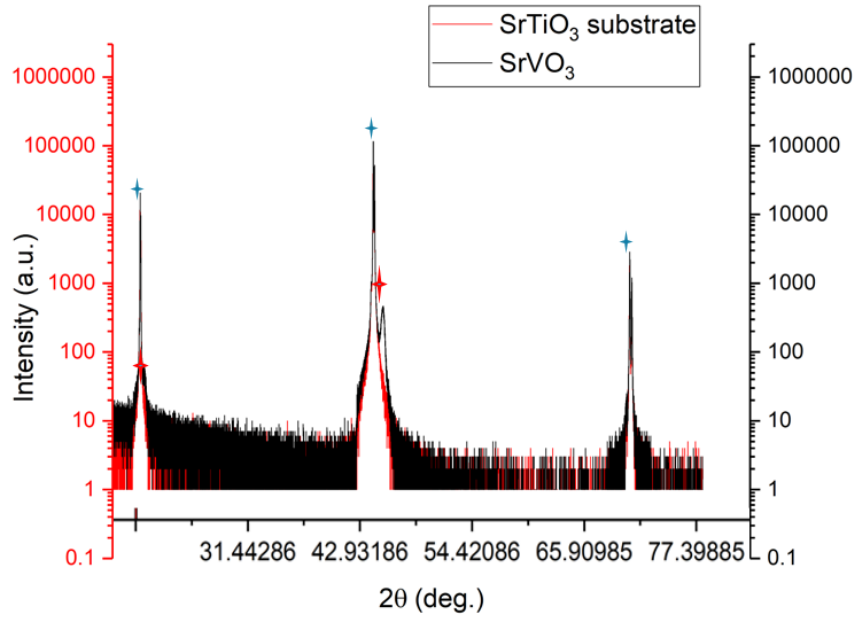


Figure 19: XPS V2p core level spectra of the sample 35/0/0 gathered by (a) standard angle measurement, (b) smaller angle measurement, fitted with V⁺⁵, V⁺⁴ and V⁺³ oxidation state peaks. Two images

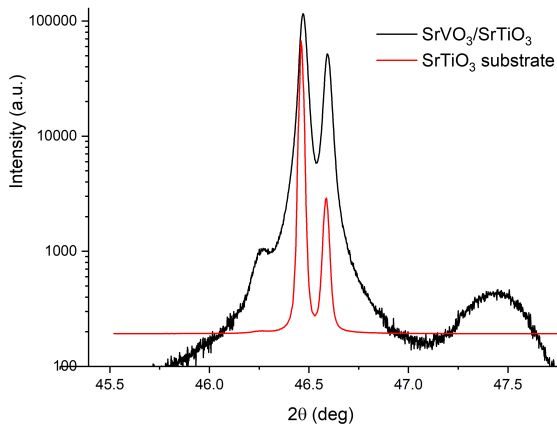
ment becomes more surface sensitive. These findings confirm the existence of a secondary, oxygen-rich phase which is located mostly at the interface.

Continuing investigation of an oxygen-rich secondary phase in SrVO₃ layers, an XRD measurement of the sample 35/0/0 is taken as presented in Figure 20. Note that the crystal structure information from the samples 2/6/2 and 2/2/2 could not be measured by XRD due to their small thickness not yielding a signal strong enough to be spotted by the detectors. XRD measurement shown in Figure 20(a) revealed the substrate peaks from SrTiO₃ marked with blue stars at positions of 2θ 22.8 (001) and 46.5 (002); in addition to relatively low intensity, broader peaks at positions 2θ 23.1 and 47.3 marked with red stars, which are assigned to (001) and (002) orientations of the cubic perovskite phase of SrVO₃. No trace of oxygen-rich, secondary phase is found in this XRD measurement. In case there was no final-state effects present in the film, 74% Nb⁺⁵ in the 14 nm SrVO₃ thin film would yield observable phase structure in XRD measurements. For this reason, it can be concluded that in addition to secondary phases present at the surface, there is final-state effects present in SrVO₃ thin film causing the appearance of multiple valence states in addition to secondary phases at the surface. The fact that secondary surface phases are not thick enough to yield additional peaks in XRD measurements is not unprecedented. Earlier, it was proven that, even though no sign of secondary phase was present in XRD measurements of SrVO₃ thin films grown by PLD under low oxygen pressure ($1.2 \cdot 10^{-6}$ mbar), would demonstrate electron diffraction patterns which prove oxygen-rich Sr₃V₂O₈ phase formed at the surface of SrVO₃. The authors noted that the lattice parameters of the hexagonal phase Sr₃V₂O₈ ($a=5.62 \text{ \AA}$, $b=5.62 \text{ \AA}$) fit nicely to the (001) of SrVO₃ in a ($\sqrt{2} \times \sqrt{2}$) surface reconstruction manner as shown in Figure 21 [8]. The same type of surface reconstruction ($\sqrt{2} \times \sqrt{2}$) at the SrVO₃ surfaces was reported to take place after deposition of thin films at 10^{-8} mbar oxygen background pressure. However, the reconstruction only claimed to cause a V⁺⁵ oxidation state at the surface and formation of a new phase was not reported [71]. In addition to these, work of Berini et al. provided AFM measurements (ex-situ) of the SrVO₃ thin films which demonstrate oblong nanostructures positioned along 011 directions of the surface. Authors assigned this precipitated phase to Sr₃V₂O₈ without providing further evidence such as elemental composition map. They also observed this secondary phase does not form if the deposition oxygen pressure of $1.2 \cdot 10^{-6}$ mbar was directly pumped down to 10^{-8} mbar after the deposition, without permitting the sample to cool down. This finding proposes that the formation of Sr₃V₂O₈ phase occurs after deposition is finished, while the sample is cooling down [8].

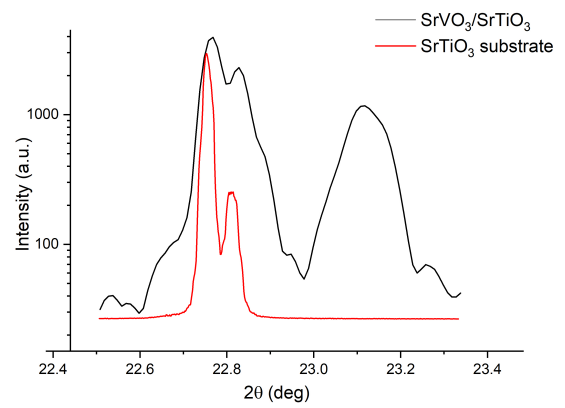
In order to investigate presence of secondary, oxygen-rich phases in samples via electron diffraction method, RHEED images of the sample 2/2/2 that are taken during and right after the growth are analyzed for clues of surface reconstruction. The reason RHEED images from the sample 35/0/0 is not presented is that, due to 3-dimensional growth, the RHEED images became unusable for the purpose



(a)



(b)



(c)

Figure 20: (a) Broad angle scan of the sample 35/0/0. The SrTiO₃ substrate (marked with blue star) and SrVO₃ (marked with red star) peaks are visible. (b) Detailed scan of the sample 35/0/0 SrVO₃ (black) compared with the SrTiO₃ substrate (red) around $2\theta=47.3$ which corresponds to (002) SrVO₃. (c) Detailed scan of the sample 35/0/0 near $2\theta=23.1$ which corresponds to (001) SrVO₃. Two images

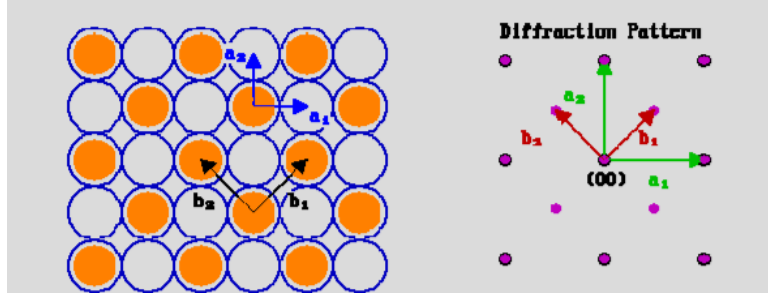


Figure 21: Demonstration of a $\sqrt{2} \times \sqrt{2}$ surface reconstruction by orange atoms. The resulting reciprocal space map showing regular (green arrow) and additional spots (red arrow) due to surface reconstruction [1].

of crystal parameter determination. As depicted in Figure 21, a ($\sqrt{2} \times \sqrt{2}$) surface reconstruction is expected to cause appearance of additional RHEED spots that are placed $1/\sqrt{2}$ closer to each other in the reciprocal space due to its inverse relationship with the real space [46]. SrVO₃ thin film at 600 C shown in Figure 22(d) proves that, apart from the pattern becoming more streaky after the deposition which is due to increased surface roughness, no significant change such as appearance of additional spots or a change in the distance between spots are found.

Note that the presented RHEED image captures the situation right after the deposition as the sample is still at 600 C. Considering the findings from Berini et al. about the surface reconstruction taking place as the sample cools down at the same pressure it is deposited, it is highly probable that the surface reconstruction has not fully taken place at the moment the RHEED image in Figure 22(d) is captured. The fact that SrVO₃ thin film structures fabricated via the same method and conditions had shown surface reconstruction after being stored in the distribution chamber for a few weeks is supporting the hypothesis that oxygen-rich phase formation occurs at the surface after the deposition, either during the cool-down or after [3]

As supportive evidence to RHEED investigation, ex-situ AFM measurement is taken. No trace from the oblong secondary phase precipitates mentioned in the work from Berini et al. is found [8]. However, Figure 28 presented in Appendices section revealed lighter color precipitates near the edges of 3-dimensional growth islands, which may indicate a secondary, oxygen-rich phase. Due to time restrictions no further elemental mapping study is done at this surface.

A decisive evidence to prove the excess³ V⁺⁵ signal is due to V surface states would be the cleaning of the SrVO₃ film surface by Ar sputtering. As explained by Lin et al. [47] in supplementary information sheet, cleaning of the SrVO₃ thin film surface reduced the amount of surface oxygen state by a factor of 3/4 and the V⁺⁵ percentage down to half of its value (the other half is proven to be due to the final-state effects). Note that even though the samples were kept under high vacuum, oxygen-rich V⁺⁵ containing phases were present [47].

Referring back to the paper by Lin et al. in which the final state effect in compounds with degenerate localized orbitals were analyzed, an optimally oxidized SrVO₃ single phase compound was reported to exhibit multiple peaks that correspond to 60% V⁺⁵, 27% V⁺⁴ and 13% V⁺³ [47]. Comparing their findings to the oxidation state distributions obtained from V 2p levels in this study, V⁺⁵ oxidation state percentage in all samples are found to be significantly high.

In the light of these findings, it is inferred that distribution of V oxidation states for the sample 35/0/0 as seen in Table 6 is partially due to final-state effects and partially due to presence of a secondary, oxygen-rich phase at the surface.

Going back to the charge transfer discussion, V valence state distributions summarized in Table 6, do not exhibit a trend in relation with $V_{\text{interface}}/V_{\text{bulk}}$ ratios. Since V receives electrons from Nb sites at the interface, it would be expected that samples 2/6/2 and 2/2/2 contains higher percentage of V⁺³ with respect to the sample 35/0/0. This apparent lack of correlation can be attributed to smearing out the meaningful trend due to the contamination of the oxidation state distributions by

³Excess amount refers to the amount which exceeds what is reported to be due to final state effects by Lin et al.

the secondary phases present at the SrVO₃ thin film surfaces.

The fact that charge transfer is still observable from Nb 3*d* core level spectra supports the hypothesis

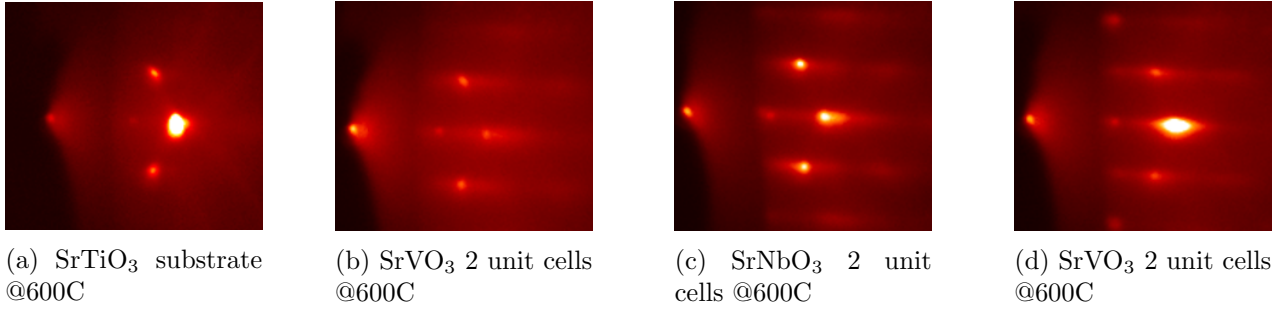


Figure 22: RHEED images taken during the deposition of the sample 2/2/2. From left to right, images follow the order of the deposition. Each image is named according to the final deposited layer, thickness and temperature. Images demonstrate conformal, epitaxial growth with constant spot separation.

that SrVO₃/SrNbO₃ interfaces are single phase, smooth and well-defined to permit the charge transfer between V and Nb sites, as supported by the RHEED images in Figure 22, and the secondary phase formation only occurs at the surface of SrVO₃ thin films.

If the time could allow further investigations in this study, capping of the SrVO₃ layer with an oxide that does not contribute to charge transfer and has comparable lattice parameters would be applied in order to observe charge transfer from V side, without interference of the secondary phases.

3.2 Charge Transfer at LaTiO₃/LaMnO₃ Interfaces

Model described in Section 1.1, predicts that, formation of an interface between (001) oriented LaTiO₃ and LaMnO₃ perovskite oxides results in sharing of oxygen octahedra at the interface and this forces oxygen 2*p* bands of LaTiO₃ and LaMnO₃ to align at the point of contact [47]. Due to this alignment, empty *d* bands of the charge transfer insulator LaMnO₃, energetically locate below the partially filled lower *d* bands of the Mott-Hubbard insulator LaTiO₃. Consequently, an electron transfer from LaTiO₃ to LaMnO₃ layer is expected to occur at the interface. According to this model, the oxidation state of Ti transition metal ion in LaTiO₃ lattice (Ti⁺³) is expected to show increasing Ti⁺⁴ character at the interface due to the charge transfer. Oxidation state of the Mn ion on the electron recipient side, LaMnO₃ on the other hand, is expected to reduce from Mn⁺³ towards Mn⁺².

In order to investigate this prediction, Mn oxidation states in two stacks which contain different Mn_{interface}/Mn_{bulk} ratios are compared with the Mn oxidation state in LaMnO₃ thin film that does not contain an interface which contributes to the charge transfer. In order to monitor a change in the oxidation state of Mn, photoelectrons gathered from Mn 2*p* and Mn 3*s* levels are utilized.

Mn 3*s* splitting values are calculated by taking the distance between the centers of the two fitted peaks. Peak fitting procedure is explained in further detail in Section 2.3.3.4. For Mn 3*s* peak splitting calculations, a regular error calculation procedure is not followed because it would contain error contributions that do not affect the peak maximum positions of Mn 3*s* and would yield meaningless results. Mn 3*s* splitting values are presented in Table 8 together with the empirically predicted Mn valence states which are calculated via Equation 6.

Results showed that the sample $(x + y)_3 + 0$, which contains $\approx 80\%$ Mn_{interface}/Mn_{bulk}, demonstrated the lowest oxidation state of Mn which is Mn^{2.41}. The sample $(x + y)_1 + 1$ which contains 100% Mn_{interface}/Mn_{bulk} on the other hand, demonstrated the second lowest oxidation state of Mn which is Mn^{+3.17}, even though the charge transfer model predicted it to be the lowest. Mn oxidation state of the sample $(x + y)_0 + 2$ which does not contain an interface⁴ is shown to be the highest (Mn^{+3.23}) since there is no transferred electron to Mn states in this sample.

⁴an interface which contributes to the charge transfer

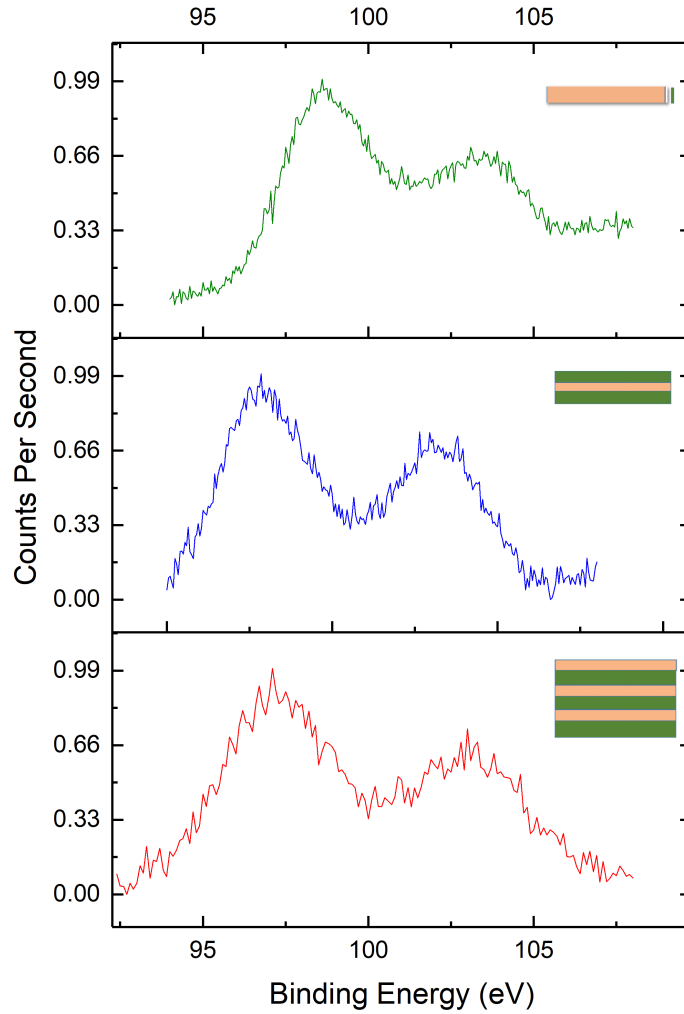


Figure 23: Mn3s core level spectra collected via standard angle XPS measurement, by using 50 eV.

Considering the $Mn_{\text{interface}}/Mn_{\text{bulk}}$ ratios of 80 % and 100% are relatively close to each other, observed oxidation state trend between samples $(x + y)_3 + 0$ and $(x + y)_1 + 1$ can be attributed to the inhomogeneous distribution of oxygen vacancies between the samples. Even though the general trend in the oxidation states is as predicted, charge transfer amount may be so low that it cannot be resolved by the minor changes of the ratio $Mn_{\text{interface}}/Mn_{\text{bulk}}$.

One limitation of this study is the lack of information about the sample stoichiometry. As explained in Section 2.3.3.3, stoichiometry calculations are only taken from samples whose thicknesses are higher than 10 nm. Due to XPS equipment break down before an XPS spectra of a 10 nm $LaMnO_3$ film is taken, the stoichiometry of the samples are speculated by analyzing the results of the empirical Equation 6.

According to these results, presence of $Mn^{+3.23}$ state in sample $(x + y)_0 + 1$ can be attributed to two causes. First cause is the presence of an oxygen-rich secondary phase which contains Mn^{+3} state or La/Mn cation offstoichiometry. Second cause is, because the empirical data source [9] that was used to create the empirical Equation 6 was containing information from solid-state synthesized, bulk oxides; the predicted numbers may not be accurate for the comparison with thin films.

Mn 2p core level spectra of the samples are presented in Figure 24(a) and (b). Note that the characteristic shape features of the Mn 2p core level spectra reveal valuable information about the Mn valency. As stated in Section 2.3.3.4 in detail, Mn 2p spectra acquire multiplet splitting proposed by Gupta et al. [23]. Since these splittings are different for Mn^{+3} and Mn^{+2} states, tailor-made peak

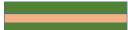
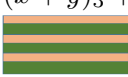
$(x + y)_n + a$	$\Delta_{\text{Mn } 3s}(\text{eV})$	Mn valence
$(x + y)_0 + 2$ 	5.07	3.23
$(x + y)_1 + 1$ 	5.12	3.17
$(x + y)_3 + 0$ 	5.72	2.41

Table 8: Mn3s peak splitting values calculated from the spectra on the left presented with corresponding Mn valence states calculated according to the Equation 6.

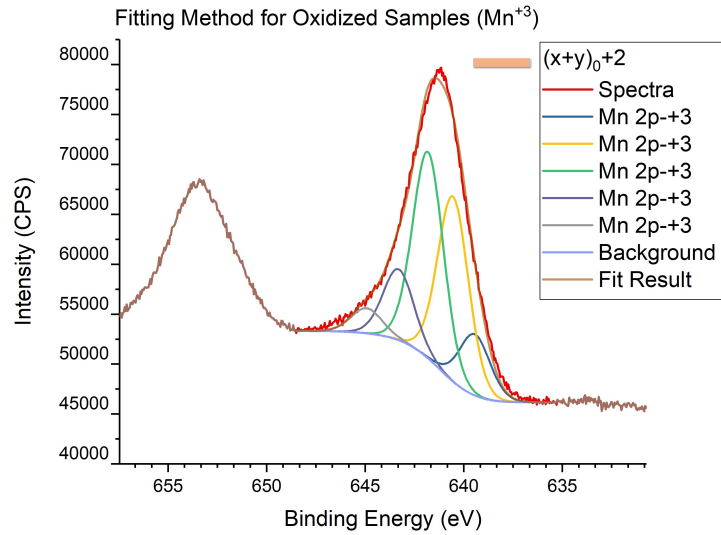
fitting models that are developed for Mn^{+2} and Mn^{+3} can be used to differentiate between the two oxidation states.

Even though differentiation between Mn^{+3} and Mn^{+2} states can be done, quantitative analysis of the two oxidation phases cannot be deduced by using this method.

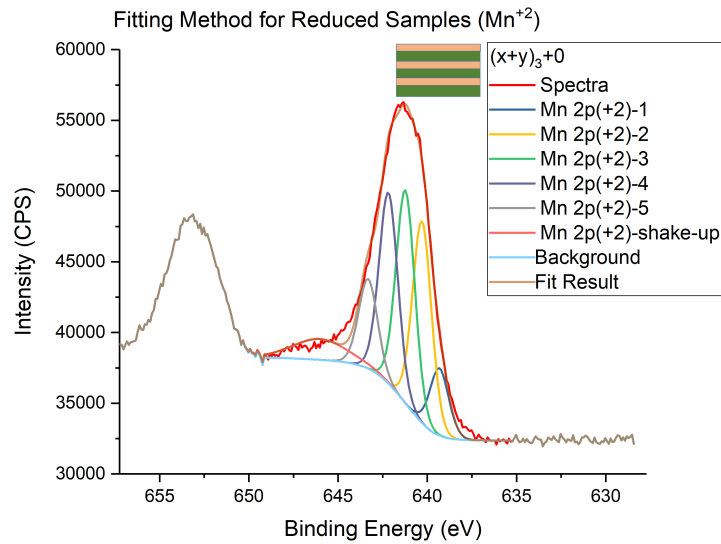
Apart from differences in the main peak structure of the Mn 2p level, appearance of a shake-up peak is expected when oxidation of the Mn becomes Mn^{+2} . Details about the shake-up peak structure is given in Section 2.3.3.4. For the sample in Figure 24(a), the model for Mn^{+3} state is used while for the sample in Figure 24(b) the model for the Mn^{+2} state is preferred. The choice of peak fitting model is done according to the expected Mn oxidation state from the samples. As seen from both figures, the peak fitting successfully filled under the real spectra except for the shake-up peak structure in Figure 24(b) which is credited with a bigger importance in the peak fitting model than what is observed at this work. The intensity of the shake-up peak in this work is found to be significantly smaller than what is observed in the work from Biesinger et al. [10]. However, there are other works in the literature in which the shake-up peak has less or no intensity contribution which is discussed in Section 2.3.3.4 in greater detail.

In order to demonstrate the difference in two peak fitting models (for Mn^{+2} and Mn^{+3}), the spectra of the sample $(x + y)_3 + 0$ tried to be fit with the model for Mn^{+3} that does not correspond to its oxidation state, the resulting fit has failed to fill under the characteristic Mn 2p spectra as shown in Appendix section Figure 29.

For a better comparison of the shake-up peak structures in the samples, Figure 25 presented the Mn 2p spectra that are normalized with respect to the total area. It clearly demonstrates that the two samples which contain $\text{LaTiO}_3/\text{LaMnO}_3$ interface: $(x + y)_1 + 1$ (blue) and $(x + y)_3 + 0$ (red) exhibited shake-up peaks positioned at binding energies of ≈ 654 eV (≈ 6 eV higher than the Mn $2p_{3/2}$ peaks), the sample $(x + y)_0 + 2$ (green) which contains solely 2 unit cells of LaMnO_3 , did not exhibit a peak formation at the expected position. It is worth noting that the sample $(x + y)_0 + 2$ demonstrated broader peak features that have higher asymmetry towards the high binding energy side. The broadening can be attributed to the fact that this measurement is taken with 50 eV pass energy, causing a decrease in the resolving quality, while the rest is taken with 20 eV. Under normal circumstances, a comparison between different pass energies is not recommended. However, since obtaining new measurements was no longer an option due to an out-of-service XPS device, the spectra is presented in current manner.



(a) The sample $(x + y)_0 + 1$. Mn2p spectra is fitted by using the peak fitting method for Mn^{+3} .



(b) The sample $(x + y)_3 + 0$. Mn2p spectra is fitted by using the peak fitting method for Mn^{+2} .

Figure 24: Mn2p core level spectra of the samples taken at 20 eV pass energy with a standard angle.

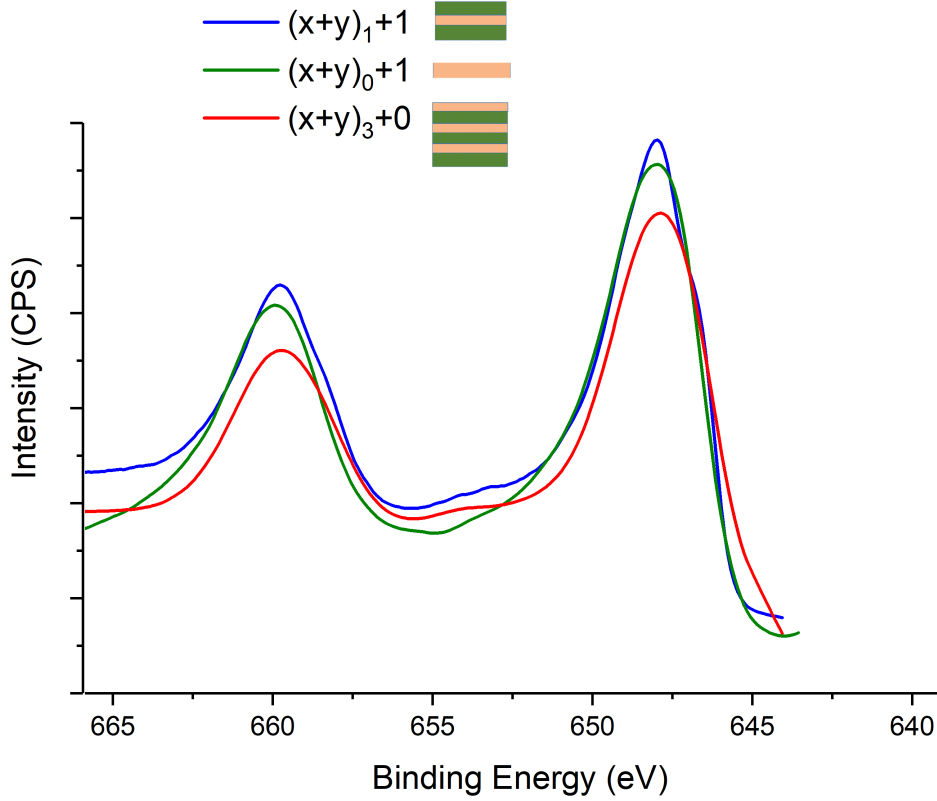


Figure 25: Mn2p core level spectra of the samples $(x+y)_1+1$ (blue), $(x+y)_0+1$ (green), $(x+y)_3+0$ (red). XPS Spectra of blue and red spectra are taken at 20eV pass energy while green is taken at 50eV. Normalization of the peaks are with respect to total area under each peak.

In order to monitor the valence state of the transition metal on the other side of the interface, Ti 2p core level spectra of LaTiO₃ containing stacks are analyzed. As mentioned earlier, due to charging effects, significant, non-homogeneous shifts are observed at the spectra. Even though the calibration of the O 1s peak to binding energy of 530 eV is done, the presented spectra differs from what is reported in the literature. For this reason, during the peak fitting procedure of the collected spectra, relative distances between the corresponding valence states are taken as reference which is explained in detail in Section 2.3.3.4.

Figure 26 demonstrates the results of the peak fitting procedure for Ti 2p core levels. Red peak which is assigned to Ti⁺⁴ state has shown to dominate the spectra. Orange peak which is assigned to Ti⁺³ state on the other hand, shown to exist in both spectra but not fully resolved. Claiming that the assigned peaks are corresponding to the correct oxidation states would be a mistake due to the following reasons. Firstly, significant charging effects made interpretation with respect to the exact peak positions impossible and the current peak fitting method explained in Section 2.3.3.4 was open to misleads by peak asymmetry or peak broadening. Secondly, since the peak assigned to represent the Ti⁺³ state is not fully resolved, there was a chance that this feature represented a secondary phase present in the material: La₂Ti₂O₇ [39]. As described in Section 2.2.4, formation of a secondary phase La₂Ti₂O₇ was frequently reported during the growth of LaTiO₃. Difficulty of resolving Ti⁺³ state was reported before [40] and the suggestion of using Scanning Transmission Electron Microscopy-Electron Energy Loss Spectroscopy (STEM-EELS) method to be able to collect information from Ti⁺³ state was proposed [25]. However, due to time limitations, additional methods to gather valence state information from Ti sites were not given a chance. In conclusion to the presented discussions, assigning oxidation states to the fitted peaks in Figure 26 is avoided. And the possibility of providing charge transfer evidence by interpretation of the Ti 2p state

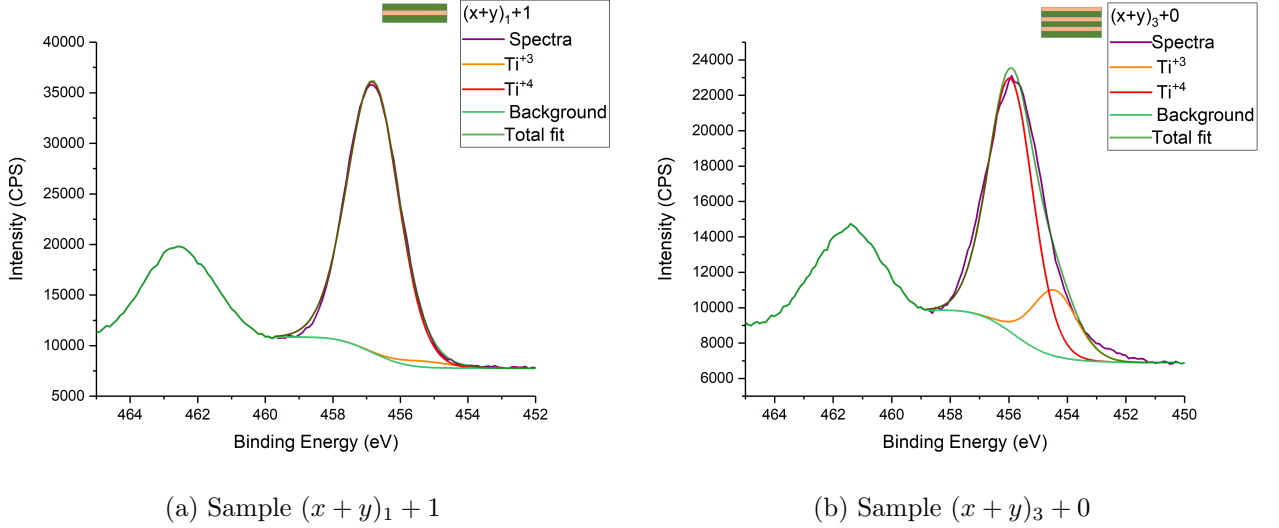


Figure 26: Ti $2p$ core level spectra taken with XPS standard angle measurement with a pass energy of 50eV. Two peaks supposedly assigned to Ti $^{+3}$ (orange) and Ti $^{+4}$ (red) are fitted under the spectra.

spectrum is discarded for this study. However, it should be noted that the decision of not utilizing the Ti $2p$ XPS data is done considering the conditions valid for this study and should not discourage the use of this technique in future studies. For instance, previously Kleibeuker et al., successfully demonstrated the charge transfer between LaTiO $_3$ and LaFeO $_3$ oxides by using XPS spectra of Fe and Ti element [39].

Conclusively, even though evidence signalling the expected shift on the Mn oxidation state from Mn $^{+3}$ to Mn $^{+2}$ is found at the interfaces, due to the characteristics of the utilized peak fitting methods, quantitative analysis on the amount of charge transfer could not be done.

4 Conclusions

4.1 Conclusions on SrVO $_3$ /SrNbO $_3$ Interface

The findings of this study suggested that the presence of a SrVO $_3$ /SrNbO $_3$ interface has significant effect on the oxidation states of the Nb transition metal sites, which are near the interface. The results in Table 5 showed that increasing the Nb $_{\text{interface}}$ /Nb $_{\text{bulk}}$ ratio of the fabricated samples caused a significant increase in the percentage of Nb $^{+5}$ oxidation state. This result was predicted from the theoretical model that, upon formation of an interface between SrNbO $_3$ and SrVO $_3$ perovskite compounds, electrons from partially filled d orbital states of Nb in SrNbO $_3$ lattice would transfer towards the empty d orbital states of V in SrVO $_3$ lattice [75].

On the other hand, as presented in Table 6, the results from the other side of the interface, which is the SrVO $_3$ layer, did not demonstrate any meaningful trend in the V oxidation state with respect to the change in V $_{\text{interface}}$ /V $_{\text{bulk}}$ ratio between samples 2/2/2 and 35/0/0, and samples 2/6/2 and 35/0/0. Presence of an oxygen rich secondary phase is concluded to account for the large fluctuations in the V $^{+5}$ states in the samples. It is believed that the noise from secondary phase smeared out the meaningful contribution from the interface V states and prevented a possible interpretation.

Angle resolved XPS measurements presented in Figure 7 as supported by literature examples [8] proved the existence of a secondary phase at the surface of the SrVO $_3$ thin films. Referring to the work by Berini et al., the formation of this secondary phase is assumed to take place while the sample was being cooled down after the deposition, because no clear evidence of the surface reconstruction was found in the RHEED image taken at 600 C (as seen in Figure 22(d)) right after the deposition, while later RHEED measurements revealed the appearance of a surface reconstruction [3].

The conclusion that the secondary phase is formed while cooling down and it is only formed at the surface of the SrVO $_3$ thin films, is supported by the fact that the observation of a charge transfer

at SrVO₃/SrNbO₃ interface still being possible due to the well preserved SrVO₃/SrNbO₃ interfaces below the surface. RHEED images gathered during the deposition of SrVO₃/SrNbO₃/SrVO₃ stack presented in Figure 22 demonstrated a well-matched interface between SrVO₃ and SrNbO₃ supporting this argument. Note that the charge transfer is assumed to be only possible through corner sharing perovskite structures that are undistorted and interfaced through their (001) plane orientations, as pointed out by Zhong et al. [74].

As a suggestion for the future work, a low energy electron diffraction (LEED) map can provide clearer evidence about the surface reconstruction since the observable reciprocal space map is 2-dimensional and the specular spot quality is more robust against streaky image formation due to the low energy of the electrons.

In the light of the conclusion that secondary phases are forming at the surface after the deposition, an insight for the future work can be the use of a capping layer to prevent the formation of the secondary phases. Even designing SrNbO₃/SrVO₃ stacks that have SrNbO₃ termination can be a solution to this problem if additional charge transfer effects between the capping layer and the stack wants to be eliminated.

4.2 Conclusions on LaTiO₃/LaMnO₃ Interface

By using XPS, two different energy spectra of the Mn element were analyzed by three different techniques and the results indicated a trend between the ratio Mn_{interface}/Mn_{bulk} and the Mn valence state. Interpreting this trend by using charge transfer model at oxide interfaces, it was concluded that the presence of a LaTiO₃/LaMnO₃ interface has a reducing effect on the Mn ions nearby since the alignment of oxygen *p* levels at the interface causes electron transfer from partially filled *d* orbitals of the Ti ion in LaTiO₃ to the partially filled *d* orbitals of the Mn ion in LaMnO₃ lattice.

Even though Mn oxidation states in high Mn_{interface}/Mn_{bulk} ratio stacks were not significantly lower than the control group (Mn⁺³ in bulk LaMnO₃), combination of different methods to measure this minor decrease consistently, lead to success in providing solid evidence.

Mn 3s splitting caused by coupling of a hole in atom's subshell to an empty valence subshell is analyzed by use of an empirically derived formula [9] which revealed that Mn sites in LaMnO₃ lattice, closer to LaTiO₃ interface, can acquire valence states down to Mn^{+2.41}. This finding is interpreted as a proof for charge transfer at interfaces.

Mn 2*p* multiplet splitting and the change of this splitting caused by Mn oxidation state are utilized to characterize Mn 2*p* peaks and qualitatively assign them to an oxidation state [23]. These qualitative indications on the valence state of the Mn element in different material stacks later on combined with the charge transfer model to interpret the effect of the interface on charge transfer. It was found that material stacks containing Mn atoms closer to the interface demonstrated Mn⁺² character which is highlighted to be due to the electron transfer from *d* orbitals of the Ti ion in LaTiO₃ to the *d* orbitals of the Mn ion in LaMnO₃ lattice.

In addition to these, Mn 2*p* shake-up peak appearance upon transition to Mn⁺² state is utilized to confirm the charge transfer. However appearance of a shake-up peak structure also remained as a qualitative method to demonstrate the charge transfer and the transferred charge per unit cell could not be calculated.

Unfortunately, XPS core level spectra of Ti 2*p*, gathered from the LaTiO₃ side of the interface could not be utilized. The main reasons behind this were: Significant non-homogeneous charging effects that could not be fully fixed via charge neutralizer making the peak fitting with respect to the specific peak positions impossible. In addition to this, the current peak fitting method explained in Section 2.3.3.4 was open to misleads by peak asymmetry or peak broadening. Lastly, since the peak assigned to represent the Ti⁺³ state is not fully resolved in the spectra, there was a chance that this feature represented a secondary phase present in the material such as La₂Ti₂O₇ [39]. As a result, possibility of providing charge transfer evidence by interpretation of the Ti 2*p* level spectrum is discarded for this study.

4.3 Suggestions for Future work

In addition to small, distributed comments about the suggestions for future work, the following topic should be considered: Since defects in crystal structure are inevitable, even though minor there will be oxygen vacancies and cation off-stoichiometry present in the fabricated samples. Because these defects have direct impact on the oxidation states of transition metal sites in TMO, low amount of charge transfers observed at the interfaces can go unnoticed due to noise from structural defects. My suggestion is to prefer a TMO pair that is more robust to defects because of the high amount of charge transfer.

In this study only physical phenomenon that was driving the charge transfer was the band alignment of d levels at the interface. So the observed change in the transition metals valence state was very small. The work of Kleibecker et al. on the other hand, in addition to the band alignment, the transition between high-spin, low-spin state in LaFeO_3 upon charge transfer which stems from crystal field splitting and Hund's exchange, caused a significant charge flow between oxides [39]. In conclusion, for the future designs, smarter TMO pair choice should be made which includes additional effects to drive the charge transfer further.

As an inclusive remark for all the interfaces studied in this work, given the small sample size, caution taken while interpreting the results.

References

- [1] Oberflaechenphysik. <https://physik.uni-paderborn.de>. Accessed: 15-08-2017.
- [2] Oxford english dictionary. <https://en.oxforddictionaries.com/definition/interface>.
- [3] Srvo3 surface reconstruction. unpublished.
- [4] KR Balasubramaniam, Y Cao, N Patel, S Havelia, PJ Cox, EC Devlin, EP Yu, BJ Close, PM Woodward, and PA Salvador. Phase and structural characterization of sr 2 nb 2 o 7 and srnbo 3 thin films grown via pulsed laser ablation in o 2 or n 2 atmospheres. *Journal of Solid State Chemistry*, 181(4):705–714, 2008.
- [5] D Banerjee and HW Nesbitt. Oxidation of aqueous cr (iii) at birnessite surfaces: Constraints on reaction mechanism. *Geochimica et Cosmochimica Acta*, 63(11):1671–1687, 1999.
- [6] D Banerjee and HW Nesbitt. Xps study of reductive dissolution of birnessite by oxalate: Rates and mechanistic aspects of dissolution and redox processes. *Geochimica et Cosmochimica Acta*, 63(19):3025–3038, 1999.
- [7] D Banerjee and HW Nesbitt. Xps study of dissolution of birnessite by humate with constraints on reaction mechanism. *Geochimica et Cosmochimica Acta*, 65(11):1703–1714, 2001.
- [8] Bruno Bérimi, Valérie Demange, Muriel Bouttemy, Elena Popova, Niels Keller, Yves Dumont, and Arnaud Fouchet. Control of high quality srvo3 electrode in oxidizing atmosphere. *Advanced Materials Interfaces*, 3(18), 2016.
- [9] Elke Beyreuther, Stefan Grafström, Lukas M Eng, Christian Thiele, and Kathrin Dörr. Xps investigation of mn valence in lanthanum manganite thin films under variation of oxygen content. *Physical Review B*, 73(15):155425, 2006.
- [10] Mark C Biesinger, Brad P Payne, Andrew P Grosvenor, Leo WM Lau, Andrea R Gerson, and Roger St C Smart. Resolving surface chemical states in xps analysis of first row transition metals, oxides and hydroxides: Cr, mn, fe, co and ni. *Applied Surface Science*, 257(7):2717–2730, 2011.
- [11] Cristina Buzea and Kevin Robbie. State of the art in thin film thickness and deposition rate monitoring sensors. *Reports on Progress in Physics*, 68(2):385, 2005.
- [12] Pei Chen, Padmanaban S Kuttipillai, Lili Wang, and Richard R Lunt. Homoepitaxial growth of metal halide crystals investigated by reflection high-energy electron diffraction. *Scientific reports*, 7:40542, 2017.
- [13] PI Cohen, GS Petrich, PR Pukite, GJ Whaley, and AS Arrott. Birth-death models of epitaxy: I. diffraction oscillations from low index surfaces. *Surface science*, 216(1-2):222–248, 1989.
- [14] Peter J Cumpson. Angle-resolved xps depth-profiling strategies. *Applied surface science*, 144:16–20, 1999.
- [15] M Cwik, T Lorenz, J Baier, R Müller, G André, F Bourée, F Lichtenberg, A Freimuth, R Schmitz, E Müller-Hartmann, et al. Crystal and magnetic structure of latio 3: Evidence for nondegenerate t 2 g orbitals. *Physical Review B*, 68(6):060401, 2003.
- [16] Frank De Groot and Akio Kotani. *Core level spectroscopy of solids*. CRC press, 2008.
- [17] M Demeter, M Neumann, and W Reichelt. Mixed-valence vanadium oxides studied by xps. *Surface Science*, 454:41–44, 2000.
- [18] Jacqueline BAA Elemans, B Van Laar, KR Van Der Veen, and BO Loopstra. The crystallographic and magnetic structures of la1- xbaxmn1- xmexo3 (me= mn or ti). *Journal of solid state chemistry*, 3(2):238–242, 1971.

- [19] Charles S Fadley. Atomic-level characterization of materials with core-and valence-level photoemission: basic phenomena and future directions. *Surface and Interface Analysis*, 40(13):1579–1605, 2008.
- [20] JC Fuggle, F Uf Hillebrecht, Z Zohierek, R Lässer, Ch Freiburg, O Gunnarsson, and K Schönhammer. Electronic structure of ce and its intermetallic compounds. *Physical Review B*, 27(12):7330, 1983.
- [21] Steven D Gardner, Gar B Hoflund, Mark R Davidson, Herbert A Laitinen, David R Schryer, and Billy T Upchurch. Catalytic behavior of noble metal/reducible oxide materials for low-temperature carbon monoxide oxidation. 2. surface characterization of gold/manganese oxide. *Langmuir*, 7(10):2140–2145, 1991.
- [22] MN Grisolia, J Varignon, G Sanchez-Santolino, A Arora, S Valencia, M Varela, R Abrudan, E Weschke, E Schierle, JE Rault, et al. Hybridization-controlled charge transfer and induced magnetism at correlated oxide interfaces. *Nature physics*, 12(5):484, 2016.
- [23] RP Gupta and SK Sen. Calculation of multiplet structure of core p-vacancy levels. ii. *Physical Review B*, 12(1):15, 1975.
- [24] Takakiyo Harigai, Song-Min Nam, Hirofumi Kakemoto, Satoshi Wada, Keisuke Saito, and Takaaki Tsurumi. Structural and dielectric properties of perovskite-type artificial superlattices. *Thin Solid Films*, 509(1):13–17, 2006.
- [25] G W J Hassink. *Two dimensional electron layers in perovskite oxides*. PhD thesis, University of Twente.
- [26] S Havelia, KR Balasubramaniam, S Spurgeon, F Cormack, and PA Salvador. Growth of $\text{La}_2\text{Ti}_2\text{O}_7$ and LaTiO_3 thin films using pulsed laser deposition. *Journal of Crystal Growth*, 310(7):1985–1990, 2008.
- [27] R Hesper, LH Tjeng, A Heeres, and GA Sawatzky. Photoemission evidence of electronic stabilization of polar surfaces in $\text{K}_3\text{C}_6\text{O}$. *Physical Review B*, 62(23):16046, 2000.
- [28] Shu-Fang Ho, S Contarini, and JW Rabalais. Ion-beam-induced chemical changes in the oxyanions (moyn-) and oxides (mox) where m= chromium, molybdenum, tungsten, vanadium, niobium and tantalum. *Journal of Physical Chemistry*, 91(18):4779–4788, 1987.
- [29] Mark Huijben, Gertjan Koster, Michelle K Kruize, Sander Wenderich, Jo Verbeeck, Sara Bals, Erik Slooten, Bo Shi, Hajo JA Molegraaf, Josee E Kleibeuker, et al. Defect engineering in oxide heterostructures by enhanced oxygen surface exchange. *Advanced functional materials*, 23(42):5240–5248, 2013.
- [30] Harold Y Hwang, Yoh Iwasa, Masashi Kawasaki, Bernhard Keimer, Naoto Nagaosa, and Yoshinori Tokura. Emergent phenomena at oxide interfaces. *Nature materials*, 11(2):103, 2012.
- [31] Ayahiko Ichimiya and Philip I Cohen. *Reflection high-energy electron diffraction*. Cambridge University Press, 2004.
- [32] Masatoshi Imada, Atsushi Fujimori, and Yoshinori Tokura. Metal-insulator transitions. *Reviews of modern physics*, 70(4):1039, 1998.
- [33] IH Inoue, O Goto, H Makino, NE Hussey, and M Ishikawa. Bandwidth control in a perovskite-type $\text{3d-1-}x\text{sr}_x\text{vo}_3$. i. evolution of the electronic properties and effective mass. *Physical Review B*, 58(8):4372, 1998.
- [34] N Ishizawa, F Marumo, T Kawamura, and M Kimura. The crystal structure of $\text{Sr}_2\text{Nb}_2\text{O}_7$, a compound with perovskite-type slabs. *Acta Crystallographica Section B: Structural Crystallography and Crystal Chemistry*, 31(7):1912–1915, 1975.

- [35] Josee Kleibeuker. *Reconstructions at complex oxide interfaces*. PhD thesis, University of Twente.
- [36] G. Johansson J. Hedman P.-F. Heden K. Hamrin U. Gelius T. Bergmark L. O. Werme R. Manne Y. Baer K. Siegbahn, C. Nordling. Effect of biaxial strain on the electrical and magnetic properties of (001) La_{0.7}Sr_{0.3}MnO₃ thin films. *ESCA Applied to Free Molecules*, 1969.
- [37] Min Kang, Eun Duck Park, Ji Man Kim, and Jae Eui Yie. Manganese oxide catalysts for NO_x reduction with NH₃ at low temperatures. *Applied catalysis A: general*, 327(2):261–269, 2007.
- [38] DH Kim, D-W Kim, BS Kang, TW Noh, DR Lee, K-B Lee, and SJ Lee. Electrical properties of SrVO₃/SrTiO₃ superlattices grown by laser molecular beam epitaxy. *Solid state communications*, 114(9):473–476, 2000.
- [39] JE Kleibeuker, Z Zhong, H Nishikawa, J Gabel, A Müller, F Pfaff, M Sing, K Held, R Claessen, Gertjan Koster, et al. Electronic reconstruction at the isopolar LaTiO₃/LaFeO₃ interface: an x-ray photoemission and density-functional theory study. *Physical review letters*, 113(23):237402, 2014.
- [40] José E Kleibeuker, Gertjan Koster, Wolter Siemons, David Dubbink, Bouwe Kuiper, Jeroen L Blok, Chan-Ho Yang, Jayakanth Ravichandran, Ramamoorthy Ramesh, Johan E ten Elshof, et al. Atomically defined rare-earth scandate crystal surfaces. *Advanced Functional Materials*, 20(20):3490–3496, 2010.
- [41] V Koerting, Qingshan Yuan, PJ Hirschfeld, T Kopp, and J Mannhart. Interface-mediated pairing in field effect devices. *Physical Review B*, 71(10):104510, 2005.
- [42] H Koinuma, M Yoshimoto, H Nagata, and T Tsukahara. Fabrication and anomalous conducting behavior of atomically regulated (SrVO₃-x)(SrTiO₃-y) superlattices. *Solid state communications*, 80(1):9–13, 1991.
- [43] Š Kos, AJ Millis, and AI Larkin. Gaussian fluctuation corrections to the BCS mean-field gap amplitude at zero temperature. *Physical Review B*, 70(21):214531, 2004.
- [44] Gertjan Koster, Boike L Kropman, Guus JHM Rijnders, Dave HA Blank, and Horst Rogalla. Quasi-ideal strontium titanate crystal surfaces through formation of strontium hydroxide. *Applied Physics Letters*, 73(20):2920–2922, 1998.
- [45] YC Lan, XL Chen, and M He. Structure, magnetic susceptibility and resistivity properties of SrVO₃. *Journal of alloys and compounds*, 354(1):95–98, 2003.
- [46] Pekka Laukkanen, Janusz Sadowski, and Mircea Guina. Surface studies by low-energy electron diffraction and reflection high-energy-electron diffraction. In *Semiconductor Research*, pages 1–21. Springer, 2012.
- [47] Chungwei Lin, Agham Posadas, Alexander Demkov, and Demkov Team. Final-state effect on x-ray photoelectron spectrum of n-doped SrTiO₃. In *APS Meeting Abstracts*, 2015.
- [48] Jochen Mannhart, David HA Blank, HY Hwang, AJ Millis, and J-M Triscone. Two-dimensional electron gases at oxide interfaces. *MRS bulletin*, 33(11):1027–1034, 2008.
- [49] Matthew SJ Marshall, David T Newell, David J Payne, Russell G Egdell, and Martin R Castell. Atomic and electronic surface structures of dopants in oxides: STM and XPS of Nb- and La-doped SrTiO₃ (001). *Physical Review B*, 83(3):035410, 2011.
- [50] Robert F Martin and Pierre-Alain Wülser. Niobium and tantalum in minerals: Siderophile, chalcophile or lithophile, and polyvalent. *Journal of Geochemical Exploration*, 147:16–25, 2014.
- [51] Zsolt Marton, Sung Seok A Seo, Takeshi Egami, and Ho Nyung Lee. Growth control of stoichiometry in LaMnO₃ epitaxial thin films by pulsed laser deposition. *Journal of Crystal Growth*, 312(20):2923–2927, 2010.

- [52] J Mendiola, R Casanova, and Y Barbaux. Xps studies of v2o5, v6o13, vo2 and v2o3. *Journal of Electron Spectroscopy and Related Phenomena*, 71(3):249–261, 1995.
- [53] D Morris, Y Dou, J Rebane, CEJ Mitchell, RG Egdell, DSL Law, A Vittadini, and M Casarin. Photoemission and stm study of the electronic structure of nb-doped tio 2. *Physical Review B*, 61(20):13445, 2000.
- [54] HW Nesbitt and D Banerjee. Interpretation of xps mn (2p) spectra of mn oxyhydroxides and constraints on the mechanism of mno2 precipitation. *American Mineralogist*, 83(3-4):305–315, 1998.
- [55] John Nichols, Xiang Gao, Shinbuhm Lee, Tricia L Meyer, John W Freeland, Valeria Lauter, Di Yi, Jian Liu, Daniel Haskel, Jonathan R Petrie, et al. Emerging magnetism and anomalous hall effect in iridate-manganite heterostructures. *Nature communications*, 7, 2016.
- [56] Milton Ohring. *Materials science of thin films*. Academic press, 2001.
- [57] A Ohtomo and HY Hwang. A high-mobility electron gas at the laaio3/srtio3 heterointerface. *Nature*, 427(6973):423, 2004.
- [58] A Ohtomo, DA Muller, JL Grazul, and HY Hwang. Epitaxial growth and electronic structure of latio x films. *Applied Physics Letters*, 80(21):3922–3924, 2002.
- [59] Akira Ohtomo, DA Muller, JL Grazul, and H Yu Hwang. Artificial charge-modulation in atomic-scale perovskite titanate superlattices. *Nature*, 419(6905):378–380, 2002.
- [60] Daichi Oka, Yasushi Hirose, Shoichiro Nakao, Tomoteru Fukumura, and Tetsuya Hasegawa. Intrinsic high electrical conductivity of stoichiometric srnb o 3 epitaxial thin films. *Physical Review B*, 92(20):205102, 2015.
- [61] Masaoki Oku, Kichinosuke Hirokawa, and Shigero Ikeda. X-ray photoelectron spectroscopy of manganese—oxygen systems. *Journal of Electron Spectroscopy and Related Phenomena*, 7(5):465–473, 1975.
- [62] P Ravindran, A Kjekshus, H Fjellvåg, Anna Delin, and Olle Eriksson. Ground-state and excited-state properties of lamno 3 from full-potential calculations. *Physical Review B*, 65(6):064445, 2002.
- [63] Nicolas Reyren, S Thiel, AD Caviglia, L Fitting Kourkoutis, G Hammerl, C Richter, CW Schneider, T Kopp, A-S Rüetschi, Didier Jaccard, et al. Superconducting interfaces between insulating oxides. *Science*, 317(5842):1196–1199, 2007.
- [64] Augustinus Josephus Helena Maria Rijnders. *The initial growth of complex oxides: study and manipulation*. University of Twente, 2001.
- [65] Guus Rijnders. *The initial growth of complex oxides: Study and Manipulation*. PhD thesis, University of Twente.
- [66] PA Salvador, A-M Haghiri-Gosnet, B Mercey, M Hervieu, and B Raveau. Growth and magnetoresistive properties of (lamno 3) m (srmo 3) n superlattices. *Applied physics letters*, 75(17):2638–2640, 1999.
- [67] GA Sawatzky and D Post. X-ray photoelectron and auger spectroscopy study of some vanadium oxides. *Physical Review B*, 20(4):1546, 1979.
- [68] WC Sheets, B Mercey, and W Prellier. Effect of charge modulation in (la vo 3) m (sr vo 3) n superlattices on the insulator-metal transition. *Applied Physics Letters*, 91(19):192102, 2007.

- [69] Geert Silversmit, Diederik Depla, Hilde Poelman, Guy B Marin, and Roger De Gryse. Determination of the v2p xps binding energies for different vanadium oxidation states (v 5+ to v 0+). *Journal of Electron Spectroscopy and Related Phenomena*, 135(2):167–175, 2004.
- [70] Roger Smart. X-ray photoelectron spectroscopy, February 2013.
- [71] M Takizawa, M Minohara, H Kumigashira, D Toyota, M Oshima, H Wadati, T Yoshida, A Fujimori, M Lippmaa, M Kawasaki, et al. Coherent and incoherent d band dispersions in srvo 3. *Physical Review B*, 80(23):235104, 2009.
- [72] Takaaki Tsurumi, Takakiyo Harigai, Daisuke Tanaka, Song-Min Nam, Hirofumi Kakemoto, Satoshi Wada, and Keisuke Saito. Artificial ferroelectricity in perovskite superlattices. *Applied physics letters*, 85(21):5016–5018, 2004.
- [73] R Uecker, B Velickov, D Klimm, R Bertram, M Bernhagen, M Rabe, M Albrecht, R Fornari, and DG Schlom. Properties of rare-earth scandate single crystals (re= nd- dy). *Journal of Crystal Growth*, 310(10):2649–2658, 2008.
- [74] Zhicheng Zhong and Philipp Hansmann. Tuning the work function in transition metal oxides and their heterostructures. *Physical Review B*, 93(23):235116, 2016.
- [75] Zhicheng Zhong and Philipp Hansmann. Band alignment and charge transfer in complex oxide interfaces. *Physical Review X*, 7(1):011023, 2017.

Sample	Nb ⁺⁵ SD %	Nb ⁺⁴ SD %	Nb ⁺³ SD %	Weighted average SD %
2/2/2/	11.8	12.3	-	11.4
2/6/2/	5.40	5.40	-	5.40
0/70/0	1.10	1.20	0.30	1.02
Sample	V ⁺⁵ SD %	V ⁺⁴ SD %	V ⁺³ SD %	Weighted average SD %
2/2/2	0.09	0.06	0.04	0.08
2/6/2	0.25	0.11	0.07	0.21
35/0/0	0.14	0.06	0.05	0.12

Table 9: Standard Deviation % for Each Oxidation State Peak

Sample	Nb ⁺⁵ / all Nb	Nb ⁺⁴ / all Nb	Nb ⁺³ / all Nb
2/2/2	16.7	16.7	-
2/6/2	7.73	7.73	-
0/70/0	1.51	1.54	1.06
Sample	V ⁺⁵ / all V	V ⁺⁴ / all V	V ⁺³ / all V
2/2/2	0.12	0.10	0.09
2/6/2	0.33	0.24	0.22
35/0/0	0.18	0.13	0.13

Table 10: Standard Deviation % for Each Oxidation State Percentage

5 Appendix

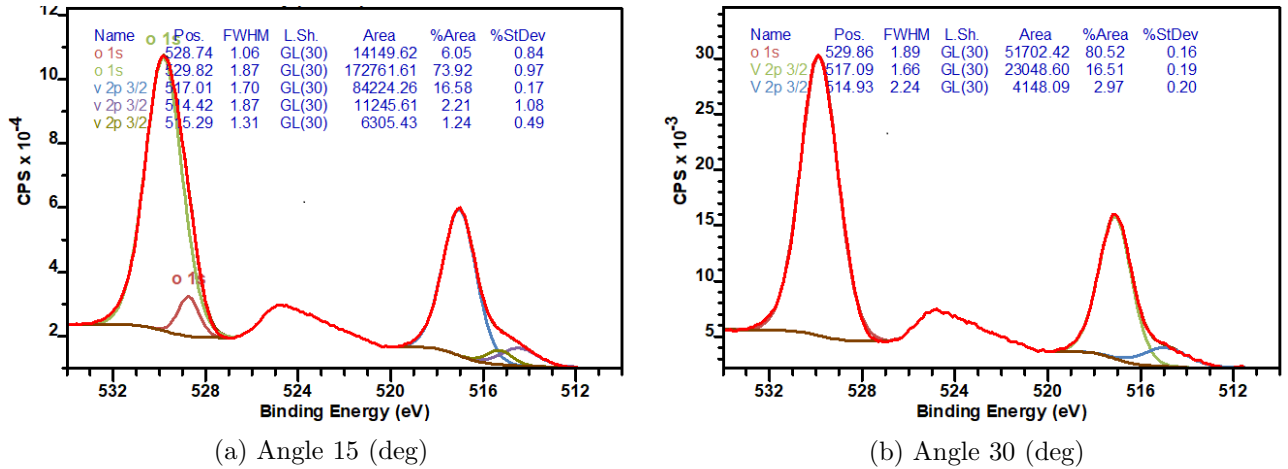


Figure 27: V2p level XPS spectra taken with two different angles (a) and (b). Fitted peaks are utilized for stoichiometry measurement.

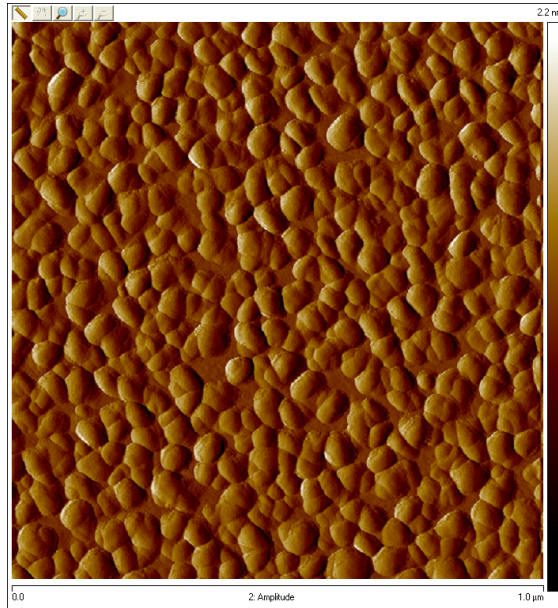


Figure 28: AFM image of the sample 70/0/0 SrVO₃ taken in non-contact mode.

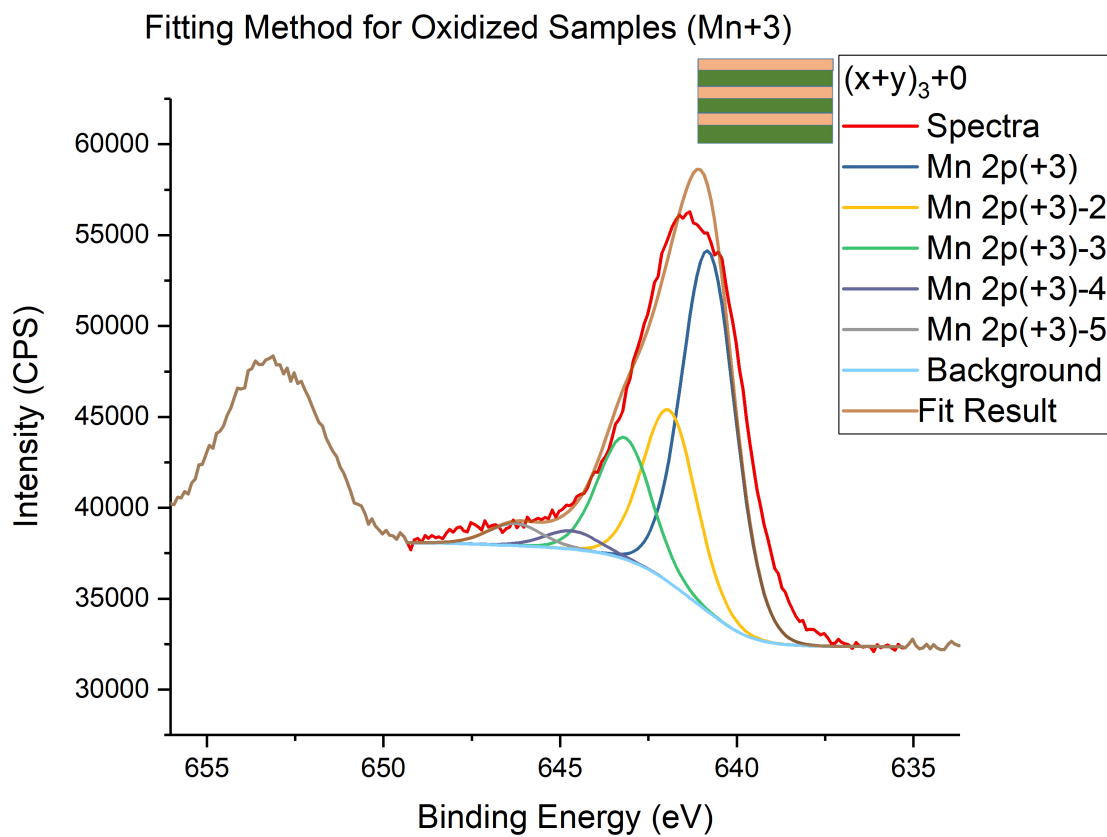


Figure 29: XPS Mn_{2p} core level spectrum of the sample. The image is presented to prove fitting model developed for Mn⁺³ state is not conforming with the peak character of this sample, which is therefore predicted to contain larger Mn⁺² character

6 Acknowledgements

I would like to acknowledge the support and guidance I received from my daily supervisor Jaap Geessinck, my supervisor Gertjan Koster and my mentor and discussion partner Jun Wang. Even though brief, I would like to thank Zhicheng Zhong for quality discussion.

In addition to this, I would like to thank Laura Vargas for teaching me to take initiative and supporting me no matter what. And Dominic Post, I would like to thank him for being a super-hero that shows up for help on a Saturday night, in case of a lab emergency even though its rainy and its 11 pm.

I would like to thank IMS family for their tireless support throughout this journey. Knowing that I can learn from peers and ask for help whenever I need give me confidence to dare new challenges.

Last but not the least I would like to thanks Andres for mental support and being a cure for my terrible grammar.